Article

Cell Reports

Mechanisms of IRF2BPL-related disorders and identification of a potential therapeutic strategy

Graphical abstract

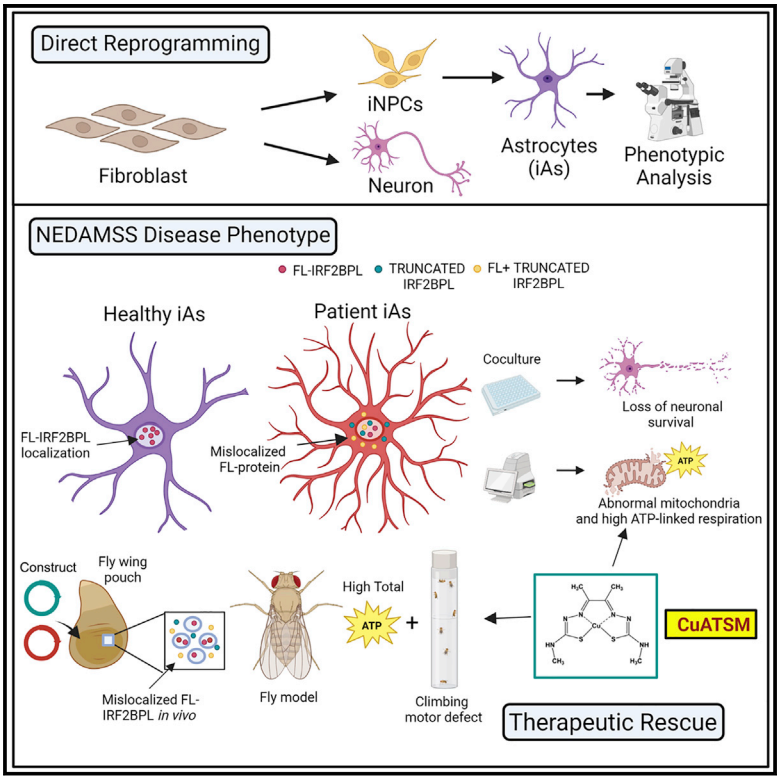

Highlights

- Description of dominant-negative mechanism of pathogenesis for NEDAMSS disease
- Mutated IRF2BPL causes mislocalization of the healthy protein form to the cytoplasm
- Astrocytes fail to perform neuronal support functions and show mitochondria defects
- CuATSM, a potential therapeutic, ameliorates disease in patient cells and a fly model

Authors

Shrestha Sinha Ray, Debdeep Dutta, Cassandra Dennys, ..., Shibi Likhite, Paul C. Marcogliese, Kathrin C. Meyer

Correspondence

kathrin.meyer@nationwidechildrens.org

In brief

Sinha Ray et al. developed a cellular model for IRF2BPL-related neurological disorder NEDAMSS, which led to identification of cytoplasmic mislocalization of full-length IRF2BPL, reduced astrocyte-mediated neuronal support, and aberrant energy household. CuATSM treatment effectively reversed some of the disease phenotypes both in patient cells and a fly model.

Sinha Ray et al., 2022, Cell Reports *41*, 111751
December 6, 2022
https://doi.org/10.1016/j.celrep.2022.111751

CellPress

Cell Reports

CellPress
OPEN ACCESS

Article

Mechanisms of IRF2BPL-related disorders and identification of a potential therapeutic strategy

Shrestha Sinha Ray,[1] Debdeep Dutta,[2,3] Cassandra Dennys,[1] Samantha Powers,[1] Florence Roussel,[1] Pawel Lisowski,[4,5,6] Petar Glažar,[4,7] Xiaojin Zhang,[1] Pipasha Biswas,[1] Joseph R. Caporale,[1] Nikolaus Rajewsky,[4] Marc Bickle,[8] Nicolas Wein,[1,9] Hugo J. Bellen,[2,3] Shibi Likhite,[1] Paul C. Marcogliese,[2,3] and Kathrin C. Meyer[1,9,10,*]

[1]Center for Gene Therapy, Abigail Wexner Research Institute at Nationwide Children's Hospital, Columbus, OH, USA
[2]Department of Molecular and Human Genetics, Baylor College of Medicine, Houston, TX, USA
[3]Jan and Dan Duncan Neurological Research Institute, Texas Children's Hospital, Houston, TX, USA
[4]The Berlin Institute for Medical Systems Biology (BIMSB), Max-Delbrück-Center for Molecular Medicine, Berlin, Germany
[5]Department of Psychiatry, Charité - Universitätmedizin Berlin, Berlin, Germany
[6]Institute of Genetics and Animal Biotechnology, Polish Academy of Sciences, Magdalenka, Poland
[7]Max Planck Institute for Molecular Genetics, Berlin, Germany
[8]Roche Institute for Translational Bioengineering, Basel, Switzerland
[9]Department of Pediatrics, The Ohio State University, Columbus, OH, USA
[10]Lead contact
*Correspondence: kathrin.meyer@nationwidechildrens.org
https://doi.org/10.1016/j.celrep.2022.111751

SUMMARY

The recently discovered neurological disorder NEDAMSS is caused by heterozygous truncations in the transcriptional regulator *IRF2BPL*. Here, we reprogram patient skin fibroblasts to astrocytes and neurons to study mechanisms of this newly described disease. While full-length IRF2BPL primarily localizes to the nucleus, truncated patient variants sequester the wild-type protein to the cytoplasm and cause aggregation. Moreover, patient astrocytes fail to support neuronal survival in coculture and exhibit aberrant mitochondria and respiratory dysfunction. Treatment with the small molecule copper ATSM (CuATSM) rescues neuronal survival and restores mitochondrial function. Importantly, the *in vitro* findings are recapitulated *in vivo*, where co-expression of full-length and truncated IRF2BPL in *Drosophila* results in cytoplasmic accumulation of full-length IRF2BPL. Moreover, flies harboring heterozygous truncations of the IRF2BPL ortholog (Pits) display progressive motor defects that are ameliorated by CuATSM treatment. Our findings provide insights into mechanisms involved in NEDAMSS and reveal a promising treatment for this severe disorder.

INTRODUCTION

IRF2BPL (interferon regulatory factor 2 binding protein-like) is an intron-less gene mapped to 14q24.3 and encodes a ubiquitously expressed transcriptional regulator belonging to the IRF2BP family.[1,2] The protein contains two highly conserved domains, an IRF2BP zinc finger DNA-binding domain and a C3HC4 RING finger domain at the N and C terminus, respectively, both involved in transcriptional modulation.[1,3] The function of the protein is largely undefined; however, several studies have shown a role in the initiation of puberty in female rodents and non-human primates as a transcriptional activator of gonadotropin releasing hormone 1 (*GNRH1*).[2,4–6] Additionally, one study has shown that IRF2BPL functions as an E3 ubiquitin ligase targeting β-catenin for proteasome degradation in gastric cancer cell lines.[7]

Recently, heterozygous truncating mutations in *IRF2BPL* have been shown to cause variable neurological phenotypes, indicating that the gene might play an important role in both development and neuronal maintenance.[8–12] Missense variants have also been reported but are mostly associated with milder neurological symptoms such as seizures, developmental delay, and autistic spectrum disorder.[8] Most severely affected individuals have typical initial development until around 3.5 years of age, at which point developmental delay and neurological regression occur, leading to abnormal movements, loss of motor skills and speech, and seizures.[8,9,12] The disorder has since been termed NEDAMSS (neurodevelopmental disorder with regression, abnormal movements, loss of speech, and seizures, MIM: 618088). Since the discovery of this disease in 2018, 25 patients have been reported worldwide[12] with *IRF2BPL* mutations causing NEDAMSS, but increased genetic testing for this rare disease will likely unravel a higher frequency.[13]

Little is known about IRF2BPL function in the nervous system. The first report to demonstrate a key role in the central nervous system showed that neuronal knockdown of *Pits*, the orthologous gene in *Drosophila melanogaster,* resulted in neurodegeneration.[8] Moreover, both human IRF2BPL and Pits cause

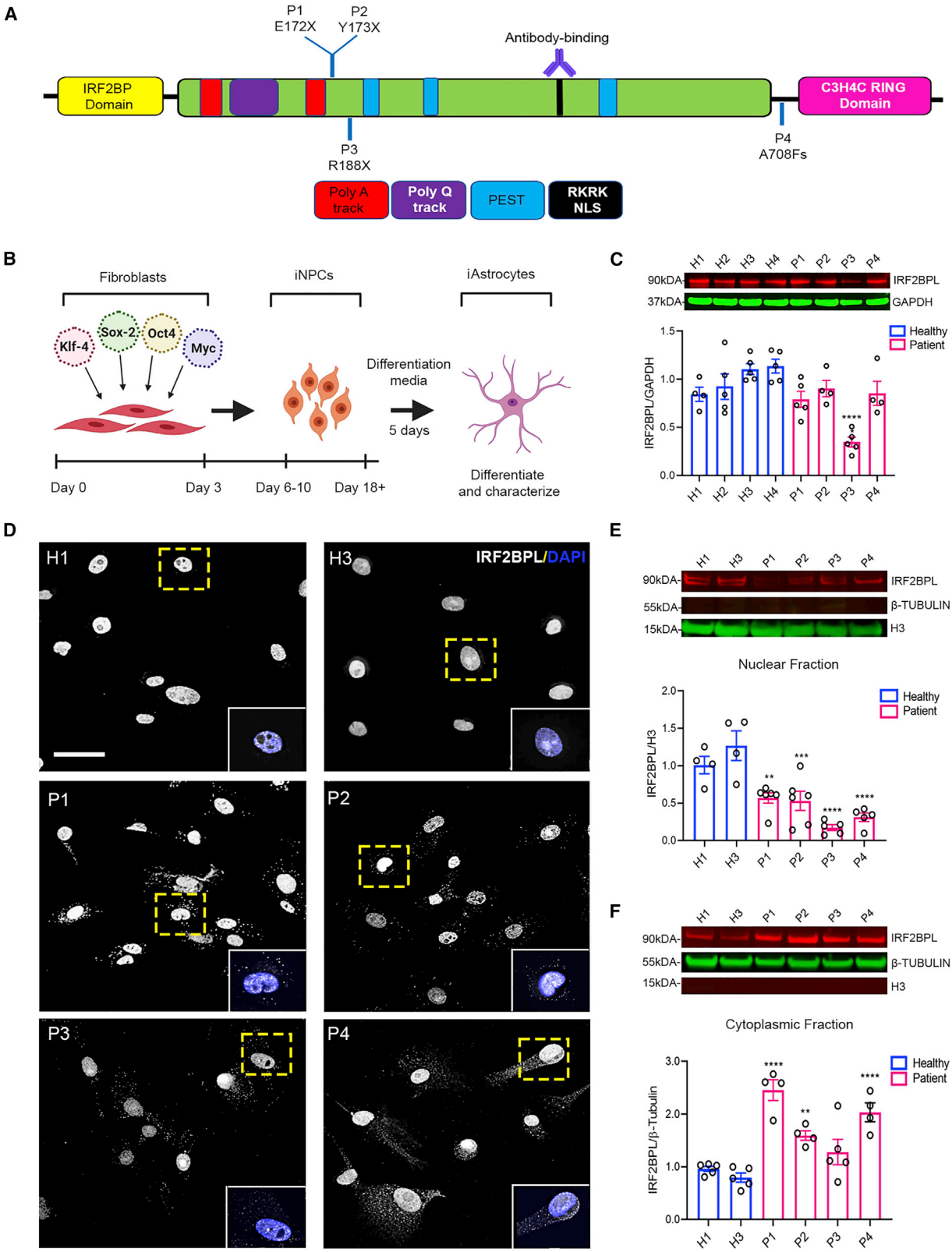

(legend on next page)

lethality when overexpressed in wild-type flies. However, overexpression of IRF2BPL truncated protein isoforms, traditionally observed in NEDAMSS patients, is not toxic in flies, which potentially implies a loss-of-function disease mechanism.[8] In addition, our recent data indicate a role for IRF2BPL/Pits in downregulating Wnt signaling in the nervous system.[14]

While loss-of-function models have been generated in non-mammalian species, the role of *IRF2BPL* in NEDAMSS has yet to be dissected in patient cells. In addition, the impact of individual patient-specific mutations or cell-type-specific contributions to NEDAMSS is currently unknown. This knowledge is critical to identify and develop a therapeutic strategy. To address these limitations, we developed a human *in vitro* cell model for NEDAMSS. Using a previously established protocol, we directly reprogrammed human patient fibroblasts into induced neurons (iNs)[15] or induced neuronal progenitor cells (iNPCs).[16] iNs from NEDAMSS patients showed variable disease phenotypes including reduced neurite length. iNPCs were subsequently differentiated into induced astrocytes (iAs), and the impact of *IRF2BPL* mutations on patient iAs was assessed. Our analyses revealed a mislocalization of IRF2BPL in the cytoplasm of patient iAs, reduced astrocyte-mediated neuronal support, and aberrant mitochondrial activity. Similar mislocalization of IRF2BPL and age-dependent defects were observed in a *Drosophila* model. Importantly, treatment with a small molecule called copper ATSM (CuATSM; diacetylbis(4-methylthiosemicarbazonato) copperII), which is currently in clinical trials for amyotrophic lateral sclerosis (ALS) (NCT04082832), successfully improved disease phenotypes *in vitro* and *in vivo* in the fly model. Hence, we propose an important role of astrocytes in NEDAMSS and describe a dominant-negative disease mechanism. Importantly, we also evaluated a potential treatment that may slow or halt the progression of NEDAMSS disease and might be applicable for other neurological conditions.

RESULTS

Full-length IRF2BPL is mislocalized to the cytoplasm in NEDAMSS patient astrocytes

To develop a human *in vitro* model for NEDAMSS, we obtained four patient fibroblast primary cell lines (Table S1) with *de novo* heterozygous mutations (confirmed by amplicon sequencing) leading to the truncation of the C3HC4 ring domain (Figure 1A). Since the disease was recently described to be caused by haploinsufficiency,[8] we first tested if these patient fibroblasts had reduced IRF2BPL protein levels by western blot analysis using a commercially available antibody that binds the nuclear localization signal (NLS) toward the C terminal of the protein (Figure 1A). This antibody detects only the full-length protein and not the truncated version, with the exception for cell line P4. Surprisingly, most patient fibroblasts showed only a small or no reduction of IRF2BPL protein levels compared with healthy controls (H1, H2, H3, and H4), and only the oldest patient (adult) P3 showed the expected ~50% loss of full-length IRF2BPL (Figure S1A). The cellular localization of IRF2BPL was established by immunofluorescence staining, and the protein was found to mainly localize to the nucleus of control fibroblasts with some signal in the cytoplasm of patient fibroblasts (Figure S1B).

Given that NEDAMSS primarily affects the nervous system and presents with various neurological symptoms in patients,[8,9,12] we explored the cell morphology and expression levels of IRF2BPL in neurons. We utilized an established direct conversion method using small molecules to generate iNs from fibroblasts.[15] After 7 days of exposure to the molecule mix, cells expressed neuronal-specific markers such as Tuj1 and Map2 (Figure S2A). Similar to fibroblasts, patient iNs mainly exhibited nuclear localization of IRF2BPL with faint signal in the cytoplasm. In contrast, in healthy control iNs, the protein was almost exclusively found in the nucleus (Figure S2B). Most patient iNs showed none or a slight reduction in IRF2BPL protein, with the exception of adult patient P3, who showed a more significant loss (Figures S2B and S2C). The mean neuronal conversion efficiency (percentage of Tuj1+ soma/DAPI) ranged between 55.9% and 73.7% for both healthy (H1 child and H3 adult) and patient iNs (P1, P2, and P4). However, the adult patient cell line P3 had a significantly lower rate of conversion (12.5%) (Figure S2D). Moreover, P3 mostly showed low Tuj1 expression in cells morphologically resembling fibroblasts, indicating incomplete conversion. Additionally, both patient iNs P1 and P3 exhibited shorter neurite length compared with healthy controls and other patient iNs (Figure S2E).

In the CNS, neurons are supported by a variety of glia. Astrocytes are the most abundant cell type in the CNS and provide a wide range of functions to support neurons. They regulate the extracellular environment of neurons, promote survival, and modulate synaptic transmission and plasticity, which are important for neuronal signaling and development[17] and frequently play an important role in disease.[18,19] To study the cellular phenotypes of NEDAMSS-derived astrocytes, patient and healthy control fibroblasts were directly converted to iNPCs and were further

Figure 1. NEDAMSS patient astrocytes show mislocalization of full-length IRF2BPL protein to the cytoplasm

(A) Illustration of IRF2BPL protein domains and the location of each patient mutation. Antibody used in study binds to the NLS, toward the C terminal of the protein.

(B and C) (B) Schematic of direct conversion of fibroblasts to iNPCs and further differentiation to astrocytes (iAs) in 5 days *in vitro*. Illustration was prepared by using biorender.com. (C) Comparison of protein quantification of healthy (H1 child and H3 adult) and NEDAMSS patient (P1, P2, P3, and P4) iAs indicates that adult patient P3 has significant loss of IRF2BPL expression.

(D–F) (D) Immunostaining demonstrates mislocalization of full-length IRF2BPL (in white) to the cytoplasm in patient iAs. Representative image was selected from 12 random (63X/Oil) fields captured by Nikon Eclipse Ti2-E. This phenomenon is further confirmed by fractionation studies with lower levels of IRF2BPL seen in the (E) nuclear fraction (normalized to nuclear marker H3) and higher amount of protein observed in the (F) cytoplasmic fraction (normalized to cytoplasmic marker β-tubulin) in patient iAs compared with healthy cell lines. ANOVA followed by Dunnett's multiple comparison test between the mean of the controls and the mean of each line was computed to derive the p value (p), *$p < 0.05$, **$p < 0.01$, ***$p < 0.001$, ****$p < 0.0001$. Yellow dotted rectangles represent the merged image of DAPI and IRF2BPL stained cell seen within the corner white boxes (dimension of image 40 μm × 50 μm) for each iAs line. The differentiation from fibroblasts to NPCs was carried out once for each cell line. All experiments were carried out on differentiated iAs with a minimum of four independent biological repeats. Scale bar represents 50 μm.

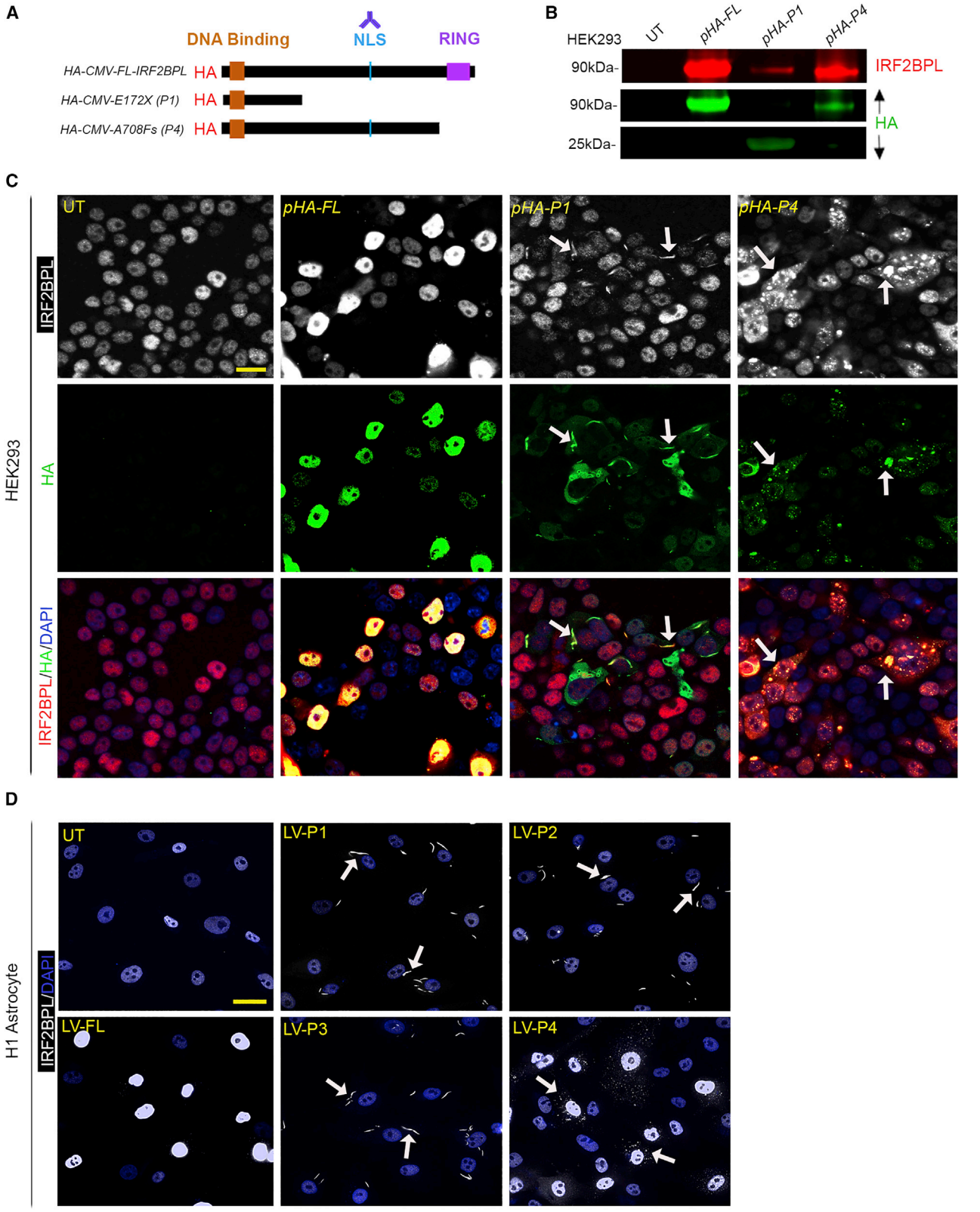

(legend on next page)

differentiated into iAs, as previously described[16,20,21] (Figure 1B). These iAs express astrocyte-specific markers such as glial fibrillary acid protein (GFAP) and CD44 (Figure S3). Interestingly, all patient iAs exhibited an activated phenotype with altered morphology and higher GFAP expression when compared with healthy controls (Figure S3). High expression of GFAP is widely accepted as a marker of activated astrocytes (reviewed in Pekny and Pekna[22]). Like previously shown in iNs and fibroblasts, western blot quantification of IRF2BPL full-length protein levels demonstrated only the adult patient P3 with significantly lower expression compared with the healthy controls (Figure 1C). Next, we evaluated the cellular localization of full-length IRF2BPL in patient iAs using immunostaining. Interestingly, full-length IRF2BPL was prominently found to be mislocalized to the cytoplasm in all four patient iAs in the form of smears or aggregated as distinct puncta (Figure 1D). To confirm these findings, nuclear and cytoplasmic fractionation followed by western blot quantification was performed. Nuclear fractions had lower levels of IRF2BPL, whereas cytoplasmic fractions had higher levels in all patient iAs compared with healthy controls (Figures 1E and 1F). These data indicate that full-length IRF2BPL is partially mislocalized to the cytoplasm in NEDAMSS patient astrocytes, and this may play a role in the disease pathogenesis.

Truncated IRF2BPL protein dimerizes with and mislocalizes full-length IRF2BPL *in vitro*

A previous study has shown that IRF2BP family proteins (IRF2BP1, IRF2BP2, and IRF2BPL) can mediate homo- or hetero-dimerization/multimerization between different IRF2BP2 family members through their conserved N-terminal IRF2BP zinc finger.[23] Hence, we hypothesized that interactions of full-length IRF2BPL with truncated forms could underlie sequestration of full-length IRF2BPL in the cytoplasm. Antibodies targeting the N terminus of IRF2BPL are currently not commercially available, and we were unable to confirm the presence of the mutant protein isoforms, but we confirmed the presence of mutated *IRF2BPL* mRNA in all patient astrocytes (Figure S4). Hence, our data suggest that the truncated RNA form of IRF2BPL in patients is stable, expressed at similar levels to the wild-type form, and does not undergo degradation. Next, we conducted HA pull-down assays to determine if full-length IRF2BPL and the mutated IRF2BPL forms found in patients can dimerize. We transfected HEK293 cells with constructs either overexpressing N-terminal HA-tagged full-length IRF2BPL (*pCMV-HA::FL-IRF2BPL*) or the HA-tagged truncated isoforms from each patient cell line (*pCMV-HA::P1/P2/P3/P4*) (Figures 2A and S5A). The pull-down assay, using protein lysate from the transfected cells, shows that IRF2BPL protein can dimerize with itself and that the truncated, tagged protein isoforms are stable. Moreover, the truncated protein forms from the patients (P1, P2, P3, and P4) can bind with endogenous full-length protein (Figures 2B and S5A). Importantly, aligned with our data from patient cells, full-length IRF2BPL was partially redistributed to the cytoplasm in the form of aggregates in HEK293 cells expressing the truncated protein forms (Figures 2C and S5B). Co-staining with antibodies against IRF2BPL and the HA tag reveals colocalization of the truncated protein with full-length protein in the cytoplasm (Figures 2C and S5B). Of note, transfection with HA-tagged truncated protein from P4 showed more protein in the pull-down assay and stronger signal of mislocalization of IRF2BPL (Figures 2B and 2C) because unlike the other mutations, the antibody can detect both the full-length and the truncated P4 protein. However, we were unable to distinguish HA-P4 and FL-IRF2BPL protein on western blot (Figure 2B) as their protein sizes (83 and 79 kDA respectively) are very similar.

Cytoplasmic sequestration of full-length IRF2BPL was also confirmed in iAs from a healthy control (H1) after infection with lentivirus overexpressing each truncated IRF2BPL protein isoforms from patients 1–4 via immunofluorescence staining (Figure 2D). Additionally, there was no overall loss of IRF2BPL upon overexpressing the mutant proteins (Figure S5D). However, fractionation studies confirmed the mislocalization phenomenon, with lower levels of IRF2BPL protein in the nuclear fraction and higher levels in the cytoplasm upon transduction with N-terminal truncated proteins (P1, P2, and P3) (Figures S5D and S5E). Interestingly, the mislocalization phenomenon on expression of truncated protein from P4 differed prominently from the other mutant proteins (Figures 2D, S5D, and S5E). Together, our data show that truncated IRF2BPL protein can dimerize with full-length IRF2BPL and sequester the protein to the cytoplasm *in vitro*. This phenomenon is seen in patient cell lines, transfected HEK293 cells, and even in healthy iAs after infection with lentiviral vectors containing the truncated isoforms.

NEDAMSS iAs fail to support neuronal viability that is rescued by CuATSM treatment

Astrocytes play a key role in providing structural and metabolic support to neurons and are responsible for the maintenance of brain homeostasis.[18,24] Since NEDAMSS patient astrocytes show aberrant morphology, increased GFAP expression, and strong redistribution of IRF2BPL from the nucleus to the cytoplasm, we assessed if these patient iAs provide proper

Figure 2. Overexpressed mutant protein interacts with full-length (FL) IRF2BPL and causes sequestration of the protein to the cytoplasm in HEK293s and in wild-type astrocyte line H1

(A) Schematic of constructs expressing N-terminal HA-tagged FL-IRF2BPL and patient truncated proteins (*HA-CMV-P1* and *HA-CMV-P4*).

(B) These constructs were transfected into HEK293s and pelleted down for HA pull-down assay after 72 h. The HA-elute blot shows untransfected (UT) cells in lane 1, HEK293s transfected with *pHA-CMV-FL-IRF2BPL* in lane 2, and *HA-CMV-P1* or *HA-CMV-P4* in lanes 3 and 4 respectively. FL-IRF2BPL (red, anti-IRF2BPL) and HA-tagged truncated variants (green, anti-HA) are seen binding to each other. The pull-down assay was performed with three independent culture replicates.

(C) Confocal imaging indicates partial mislocalization of FL-IRF2BPL to the cytoplasm in HEK293 cells transfected with the constructs overexpressing HA-tagged patient-truncated variants. White arrows point to FL-IRF2BPL proteins mislocalized to the cytoplasm. Two-dimensional images were captured at 63X/1.4 Oil magnification covering nine random fields from three independent culture replicates.

(D) Healthy H1 astrocytes transduced with lentivirus overexpressing the truncated isoform of IRF2BPL from each patient show similar sequestration of the full-length protein to the cytoplasm. White arrows point to FL-IRF2BPL protein mislocalized to the cytoplasm. Representative image was selected from 12 random (63X/Oil) fields captured from three independent culture replicates by Nikon Eclipse Ti2-E. Scale bar represents 50 μm.

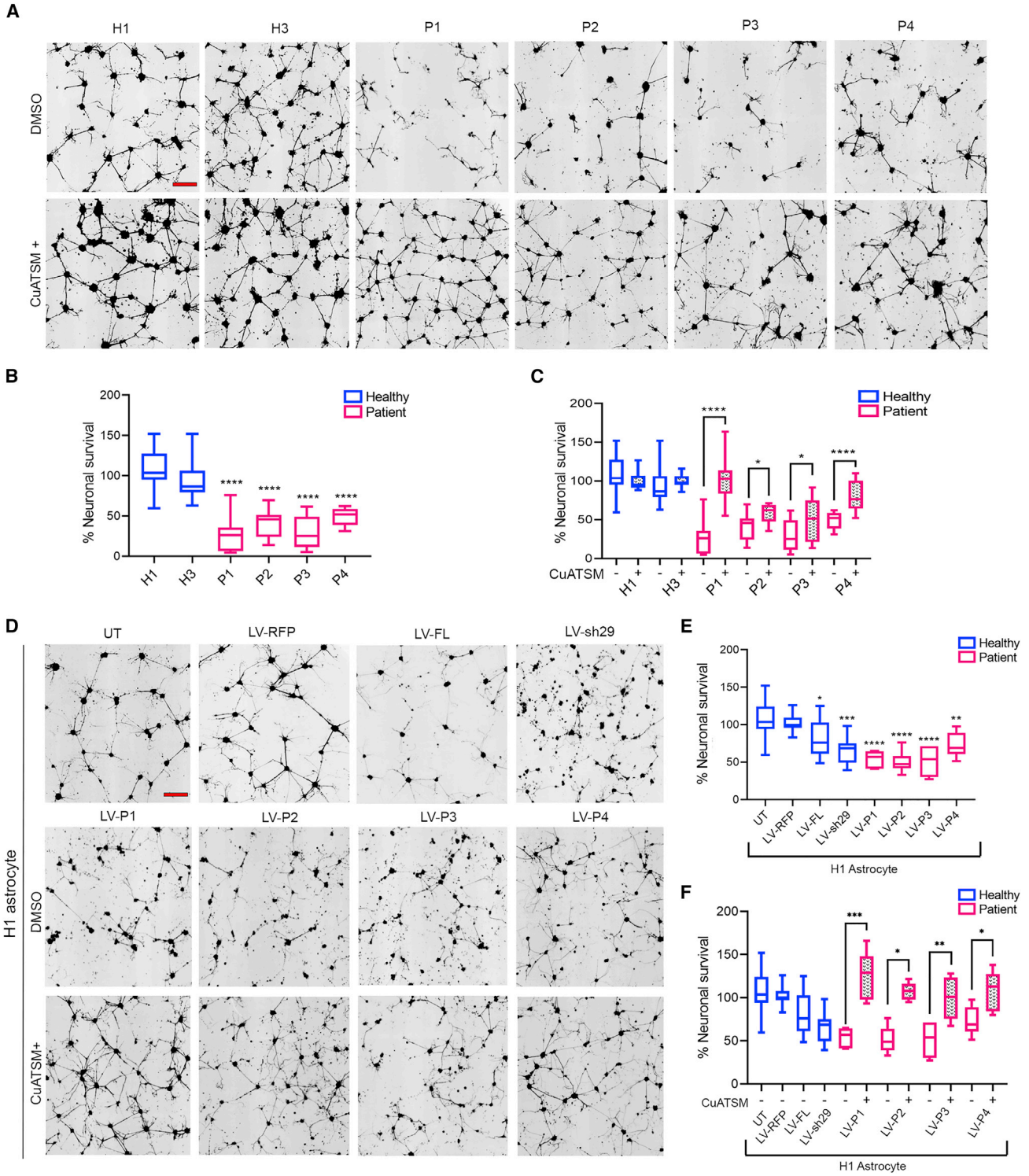

Figure 3. NEDAMSS patient astrocytes fail to support neurons, and CuATSM treatment improves neuronal survival

(A) Representative images of GFP+ mouse neurons (shown in black) following 3 days in coculture with healthy and patient iAs. The iAs were treated with either CuATSM (1 μM) or equal volume of DMSO, beginning day 2 of differentiation.

(B) Quantification of neuronal survival on day 3 shows patient iAs fail to support neurons.

(C) CuATSM treatment significantly improves neuron viability in patient lines. Data were normalized to average neuronal survival of healthy controls and represent a minimum of four independent experiments. The same DMSO-treated cell lines from (B) were used for the comparison.

(legend continued on next page)

neuronal support. We conducted coculture assays, as previously described, by co-culturing GFP+ mouse neurons on a monolayer of healthy or patient iAs.[16] After 3 days of coculture, we performed fully automated high-throughput analysis of neuronal survival. We found that neurons cocultured with patient iAs had significantly lower rates of survival than neurons cocultured with healthy iAs (Figures 3A and 3B). In our previous study involving coculture assays with ALS astrocytes, we had observed a similar loss of neuronal viability, and treatment with CuATSM drug significantly improved the survival in certain responding patient lines.[25] CuATSM is a small artificial drug currently being used in clinical trials for ALS[26,27] and Parkinson's disease (PD) (NCT03204929).[26–28] Interestingly, all patient-derived iAs treated with 1 μM CuATSM for 4 consecutive days prior to neuron-glia coculture displayed significantly increased neuronal survival (Figures 3A and 3C). However, treatment with CuATSM did not rescue the mislocalization of IRF2BPL to the cytoplasm in patient iAs (Figure S6).

Next, we investigated whether loss of IRF2BPL in astrocytes was responsible for reduced neuronal survival in coculture, hypothesizing that the cytoplasmic redistribution seen in patient cell lines leads to reduced availability of the protein in the nucleus, which could mimic a loss of function. We developed a lentivirus-expressing shRNA (LV-sh29) against IRF2BPL that could knock down approximately 50% of the protein in healthy iAs (H1) after 4 days *in vitro* (Figure S7A). H1 iAs were transduced with control or shRNA lentivirus 48 h prior to coculture with GFP+ neurons (Figure S7B). After 3 days of coculture, healthy iAs transduced with LV-sh29 showed a significant loss of GFP+ neuronal survival compared with iAs transduced with LV-RFP. Moreover, overexpression of IRF2BPL (LV-FL-IRF2BPL) in the healthy cell line also showed a slight reduction in neuronal survival (Figures 3D and 3E). Importantly, overexpressing truncated IRF2BPL proteins (LV-P1, LV-P2, LV-P3, and LV-P4) in healthy iAs decreased neuronal survival in coculture assays in a similar manner as the cells that were transduced with the shRNA construct. This indicates that the sequestration by the mutated protein acts similar to a loss of function and that the nuclear localization of the protein is key for its function (Figures 3D and 3E). We also evaluated if iAs from severe patients (P1, P2, and P3) release any toxic factors by culturing neurons with their condition media for 48 h. No significant loss of neurons was observed compared with the controls (Figures S8A and S8B). As previously seen in the patient iAs, treating the healthy iAs expressing mutant forms of the protein with 1 μM CuATSM 2 days after transduction with the lentiviral constructs significantly improved neuronal viability (Figures S7B, 3D, and 3F).

In summary, NEDAMSS iAs and healthy iAs forced to overexpress mutated versions of IRF2BPL lack neuro-supportive function, which can be rescued by treatment with CuATSM. Our data also suggest a loss-of-function mechanism for the disease, resulting from dominant-negative mutations that cause sequestration of the full-length protein from the nucleus into the cytoplasm.

NEDAMSS patient-derived iAs display aberrant mitochondrial respiration that is rescued by CuATSM treatment

Since CuATSM showed a beneficial effect without rescuing the mislocalization, we evaluated additional potential disease pathways known to be impacted by CuATSM treatment. Mitochondrial abnormalities and dysfunction are common in many neurodegenerative diseases such as ALS, PD, Alzheimer's disease (AD), and Huntington's disease (HD).[29] Moreover, CuATSM is thought to exert neuroprotective effects via a mitochondrial mechanism.[30,31] To examine if NEDAMSS iAs display alterations in mitochondrial function, we evaluated the expression of cytochrome *c* oxidase subunit 4 (COX IV), a mitochondrial marker involved in the electron transport chain.[32] In all patient iAs, COX IV showed altered localization, indicating a reduced mitochondrial network with accumulation around the nucleus (Figure 4A). However, no change in protein expression levels was observed compared with healthy controls (Figure S9A). Blinded computational analysis of the number of mitochondria per cell compared with healthy controls revealed significantly lower number of mitochondria in patient P1 and significantly higher number in P4 (Figure 4B). Interestingly, all patient iAs had a significantly higher fractionation index in comparison to healthy controls (Figure 4C), indicating a more fragmented mitochondrial network that is commonly seen in disease states.[33,34]

Based on the above observations, we next evaluated the functionality of mitochondria by conducting Seahorse ATP real-time rate assay. All patient iAs, except P1, exhibited higher levels of base oxygen consumption rate and ATP-linked mitochondrial respiration, which was measured following inhibition of ATP synthase using oligomycin (Figures 4D and 4E). The non-mitochondrial respiration was subtracted from the readings by using a mixture of rotenone and antimycin C in the assay (Figure S9B). Remarkably, treating patient P2, P3, and P4 iAs with CuATSM reduced the high levels of respiration to normal control levels (Figures 4D and 4E). Together, our data show that NEDAMSS patient iAs have aberrant mitochondrial networks and elevated levels of mitochondrial respiration (except in patient P1). Importantly, CuATSM treatment can rescue the abnormal respiration levels.

Genes involved in neuronal development and mitochondrial function are differentially expressed in NEDAMSS astrocytes

Given the role of IRF2BPL as a DNA-binding protein in transcription,[1,2] we determined the global changes in gene expression in

(D) Representative images of GFP+ neurons following coculture with H1 astrocytes un-transduced or transduced with lentivirus expressing RFP, FL-IRF2BPL, shRNA against IRF2BPL, or truncated patient (P1, P2, P3, and P4) IRF2BPL protein with DMSO or CuATSM treatment.

(E) Quantification of neuronal survival shows significant loss in viability upon overexpression, loss, or mislocalization of IRF2BPL.

(F) Treatment with CuATSM ameliorates the effect in healthy iAs transduced with truncated proteins. The same DMSO treated cell lines from (E) were used for the comparison. Data were normalized to wild-type un-transduced (UT) H1 astrocytes. ANOVA followed by Dunnett's multiple comparison test between the mean of the controls and the mean of each line was computed to derive the significance (p value). Significance between the treated and the untreated groups was computed using unpaired t tests. A minimum of three different culture repeats was used. *$p < 0.05$, **$p < 0.01$, ***$p < 0.001$, ****$p < 0.0001$. Scale bar represents 200 μm.

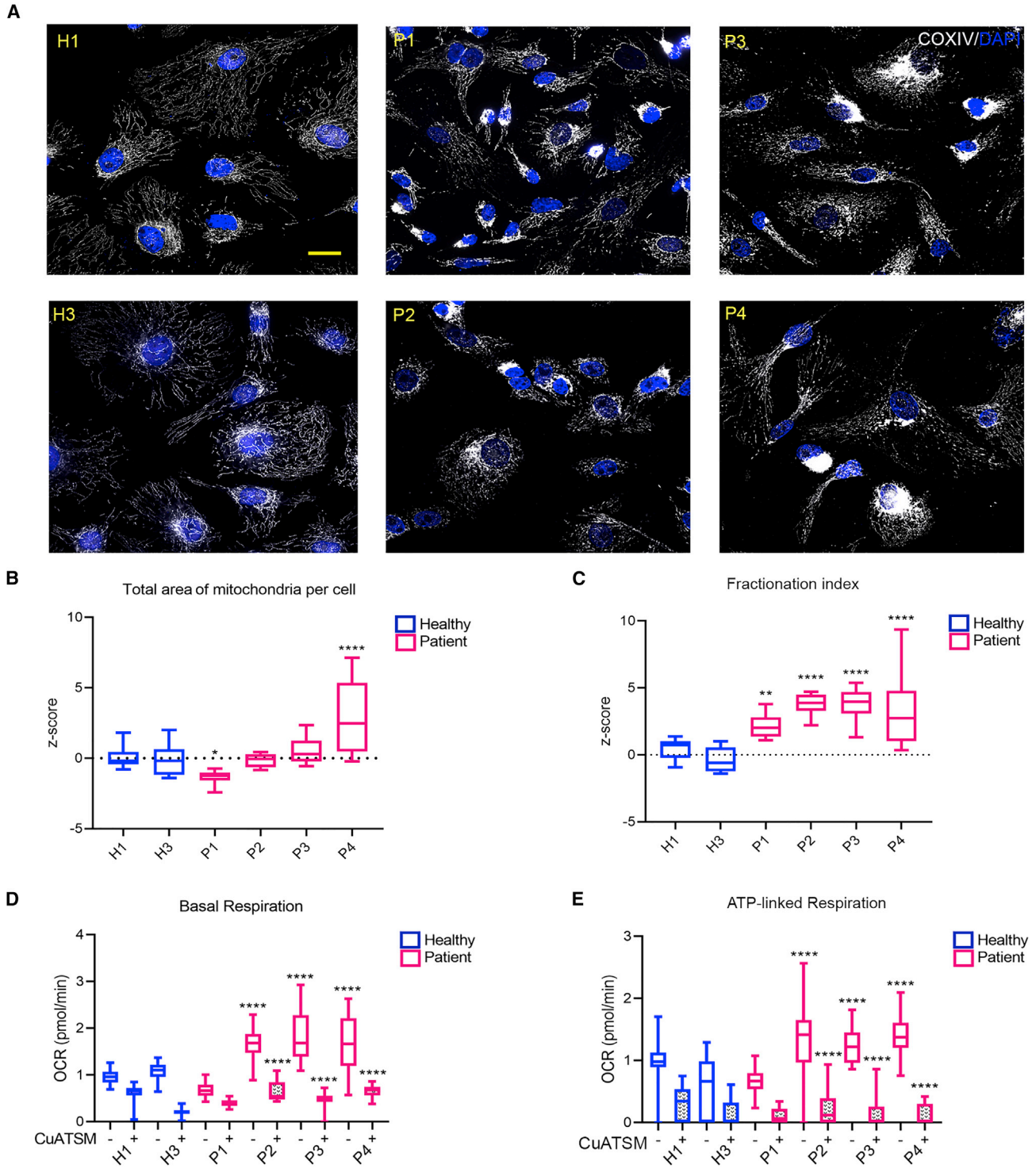

Figure 4. NEDAMSS astrocytes display aberrant mitochondrial function that is rescued by CuATSM

(A and B) (A) Patient iAs showed altered localization of COXIV (mitochondrial marker), indicating a reduced mitochondrial network with accumulation around the nucleus. Nikon Eclipse Ti2-E fluorescent images were captured at 63X/Oil magnifications, and a representative image was selected from 15 random fields, from three independent culture repeats. Computational analysis of the mitochondria revealed (B) a significantly lower number of mitochondria per cell in patient P1 and higher in patient P4.

(legend continued on next page)

NEDAMSS-associated iAs. We compared the transcription profiles of patient and healthy iAs and found 37 genes differentially expressed in all patient cell lines compared with the healthy controls (Figure 5A and Table S2). We performed computational analysis and a non-exhaustive review of the function of these genes and classified them into two functional groups relating to our *in vitro* experimental findings (Table S3). We show gene assignments to these groups with brief evidence from the literature supporting the assignments. Specifically, 19 genes are involved in neuronal growth, development, function, and support, and seven are associated with mitochondrial function, development, and/or metabolism (Figure 5A and Table S3). Of these genes, we particularly identified *SSTR2*, *ERG2, AKT3*, and *NRG2* as functionally important in both capacities and validated their differential expression between patients and controls through qPCR (Figure 5B). However, CuATSM treatment did not alter the expression of the 37 differentially expressed genes identified between patients and controls (Table S4). Moreover, gene expression changes do occur in a different manner between individual patient cell lines, indicating a patient-specific effect of the *IRF2BPL* mutations. Importantly, CuATSM improvements in phenotype are associated with mutation-specific gene expression changes that normalize the overall gene expression profile of each patient cell line rather than affecting a global disease-specific gene expression pattern (Figure 5C).

Full-length IRF2BPL is sequestered to the cytoplasm upon co-expression with truncated IRF2BPL *in vivo*

To determine if NEDAMSS-associated truncations in IRF2BPL lead to sequestration of the full-length IRF2BPL in the cytoplasm *in vivo*, we expressed untagged human *IRF2BPL* and the NEDAMSS-related truncation, *IRF2BPL*$^{p.E172X}$*::HA* (*P1::HA*), in the pouch region of the developing wing-disc of the fruit fly using the GAL4-UAS system[35] (Figures 6A and S10A). Expression of full-length IRF2BPL alone leads to the localization of this protein predominantly in the nucleus (Figure S10A). In contrast, expression of the *P1::HA* reveals punctate cytoplasmic distribution (Figures 6B and S10A). Upon co-expression, we observed that full-length IRF2BPL protein partially colocalizes with the truncated form of IRF2BPL in the cytoplasm (Figure 6B). These data further confirm that the truncated IRF2BPL can sequester some of the full-length protein into the cytoplasm *in vivo*.

To examine if heterozygous truncations in *IRF2BPL* can affect full-length function *in vivo,* we performed genetic interaction studies in flies. The overexpression of *IRF2BPL* using the glia cell promoter, *Repo-GAL4*, results in pupal lethality at 29°C (Figure S10B). Importantly, overexpression of the fly ortholog, *Pits*, in glia, also leads to pupal lethality, showing conserved function (Figure S10B). In contrast, glial expression of *P1::HA* results in viable adult flies. However, co-expression of full-length *IRF2BPL* and *P1::HA* causes both third instar larval and pupal lethality. This earlier lethality suggests the interaction of NEDAMSS-related truncated IRF2BPL and full-length protein could be toxic *in vivo*.

CuATSM treatment is protective in a *Drosophila* model of loss of IRF2BPL

The fly ortholog, *Pits*, is the single IRF2BP family member in the *Drosophila* genome and is essential in flies, as *Pits*^{TG4} mutants (a *GAL4* insertion in *Pits*) are homozygous lethal.[8] This allele splices in a cassette containing a splice acceptor (SA)-T2A-GAL4-polyA,[36,37] resulting in the premature truncation of the endogenous *Pits* gene (Figure 6C). Therefore, to mimic the human condition, we characterized heterozygous *Pits*^{TG4}/+ flies that express one full-length copy of Pits as well as a truncated form. As a control line, we used the heterozygous *Pits*^{MiMIC}/+ flies[38] (Figure 6C). Critically, *Pits*^{MiMIC} flies act as an ideal control for these experiments as they harbor a non-mutagenetic cassette in the same location as *Pits*^{TG4}, and they are homozygous viable. Due to unavailability of antibodies against Pits, we could not assess for mislocalization of the fly protein.

Interestingly, in accordance with our *in vitro* results, these *Pits*^{TG4}/+ flies display increased ATP production in flies aged 35 days post eclosion (d.p.e), while no change in total ATP levels was observed in younger flies aged 15 d.p.e. (Figure 6D). The partial loss of Pits by neuronal knockdown using RNAi is known to cause progressive climbing defects in flies.[8] In line with this, *Pits*^{TG4}/+ flies show increased time to climb in the negative geotaxis assay at 35 d.p.e. Climbing defects were not observed at 25 d.p.e., indicating an age-dependent effect (Figure 6E). Next, we determined if CuATSM provided in fly food ameliorates the climbing defects observed in 35-day-old flies. 35-day-old *Pits*^{TG4}/+ flies treated with CuATSM display decreased time to climb compared with DMSO-treated animals, indicating that CuATSM can suppress the climbing defects in these flies (Figure 6F). Together, similar to our results in NEDAMSS patient cells, partial loss of Pits in flies leads to functional deficits that can be partially rescued by CuATSM treatment, further underlining the potential of this small molecule for treatment of NEDAMSS.

DISCUSSION

Since the recent discovery of NEDAMSS, several new cases and phenotypes in patients have been documented.[8–12,39,40] Moreover, models in fruit flies and zebrafish have highlighted a role for IRF2BPL in neuronal function and maintenance.[14] These models focus on IRF2BPL loss of function, whereas in attempts to offer insight on the mechanism of action of truncating alleles, we focus on human patient cells carrying NEDAMSS truncations.

(C) All patients exhibit fragmented mitochondrial network compared with healthy iAs. The "fractionation index" parameter measured is proportional to how fractionated the mitochondrial network was. The computation was conducted on nine image fields for each line taken by Nikon microscope at 40× magnification. The analysis was conducted for three separate biological repeats, and a minimum of 20 cells were analyzed per n.
(D) The base oxygen consumption rate was measured and plotted at three timepoints for healthy, patient, and respective CuATSM-treated iAs.
(E) ATP-linked respiration was also measured following ATP synthase shutdown using oligomycin drug and subtracting the oligo OCR from basal OCR. Data represent a minimum of three independent experiments with different cultures. ANOVA followed by Dunnett's multiple comparison test between the mean of the controls and the mean of each line was computed to derive the p value (p). Significance between the treated and the untreated groups was computed using unpaired t tests. *p < 0.05, **p < 0.01, ***p < 0.001, ****p < 0.0001. Scale bar represents 50 μm.

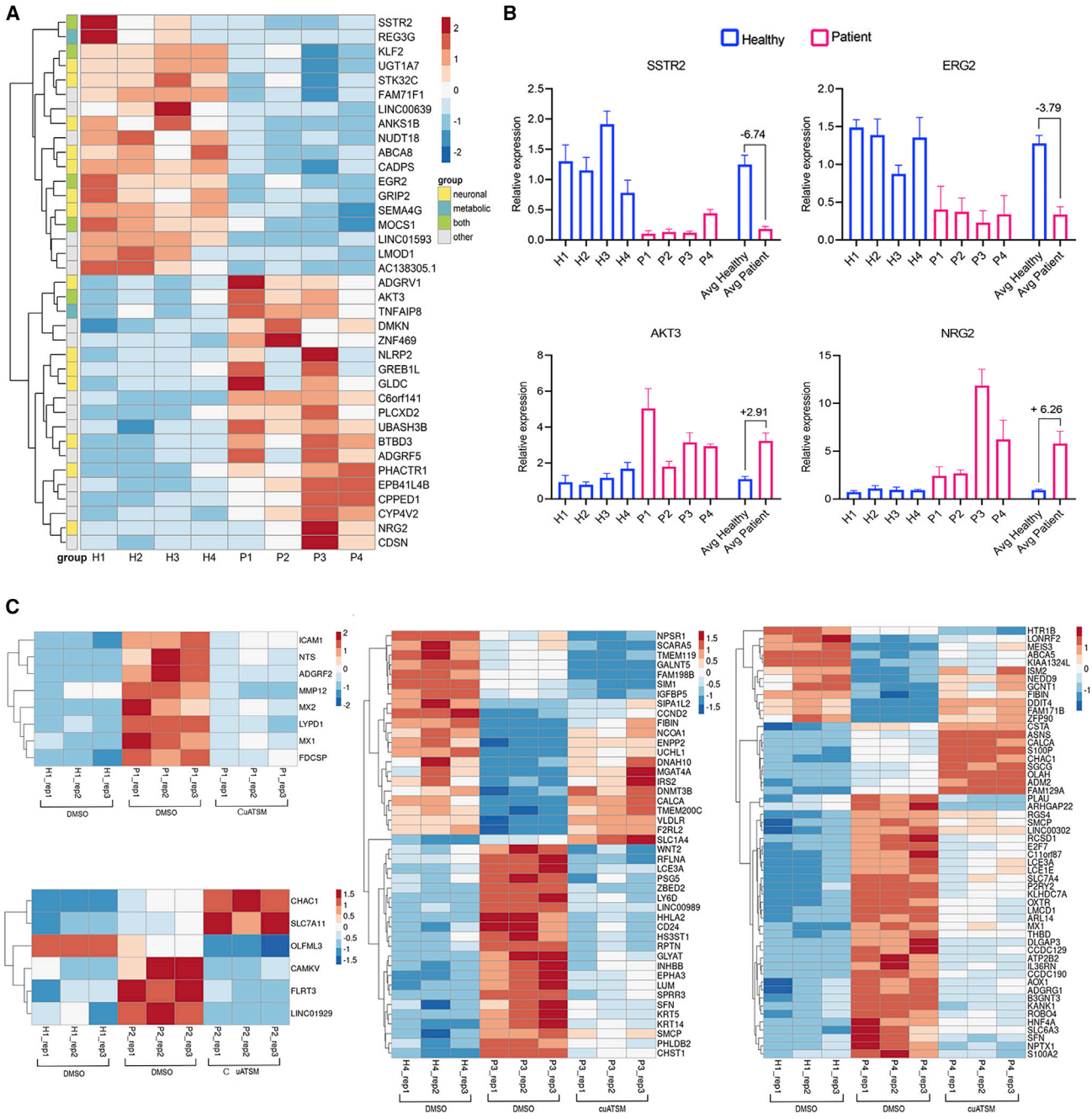

Figure 5. Neuronal growth and mitochondrial genes are differentially expressed in patient astrocytes

(A) RNA-seq analysis revealed 37 genes systematically dysregulated between patient and healthy control astrocytes. Gene expression measures were transformed to *Z* scores. Gene ontology was computed to group the genes into "neuronal," "metabolic," "both," or "other" categories.

(B) Quantitative PCR analysis of healthy and patient iAs was conducted to validate the gene expression of *SSTR2*, *ERG2*, *AKT3*, and *NRG2*. A minimum of three independent culture repeats was used for the experiment. The fold change was calculated by dividing either the average of healthy to the average of patient for downregulated genes or vice versa for upregulated genes.

(C) Heat maps depicting differentially expressed genes in patients P1, P2, P3, and P4 compared with healthy boy H1 or healthy male H4, reverted to normal levels by CuATSM. Gene expression was transformed to *Z* scores, row-wise.

Here, we have developed an *in vitro* disease model for NEDAMSS using direct conversion methods to efficiently reprogram patient fibroblasts to neurons or neuronal progenitor cells, which are further differentiated to iAs as previously described.[15,16] Direct reprogramming to model neurological disorders has several advantages over traditional iPSC method

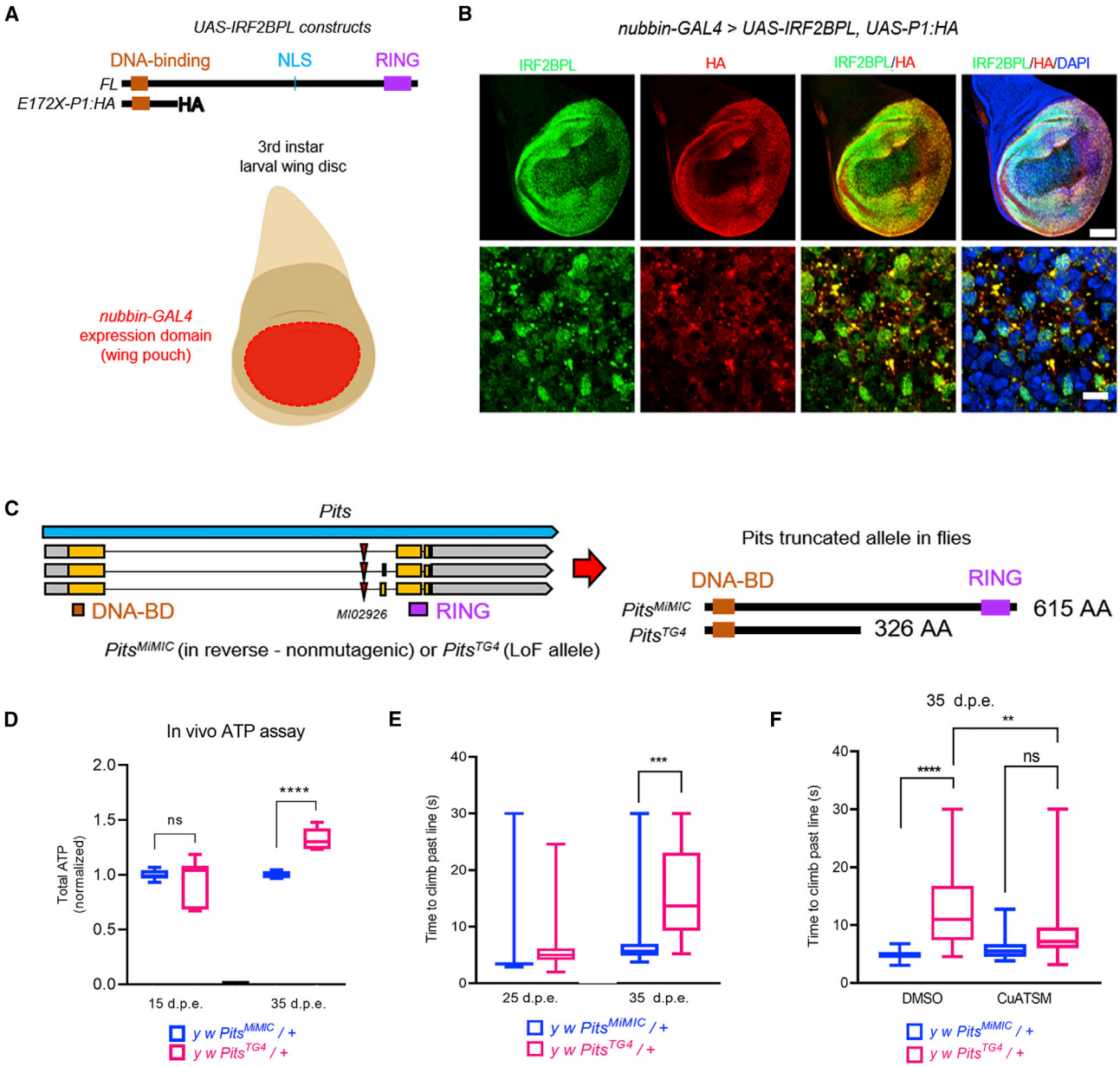

Figure 6. Truncated IRF2BPL can sequester full-length IRF2BPL in the cytoplasm *in vivo*

(A) Schematic of full-length *UAS-IRF2BPL* and truncated *UAS-p.E172X::HA* (*UAS-P1:HA*) constructs co-expressed in the developing fruit fly wing pouch (red) with *nubbin-GAL4*.

(B) Subcellular localization of full-length and truncated IRF2BPL. Full length is primarily nuclear, and the *P1::HA* construct resides in the cytoplasm. Co-expression of both full-length and truncated IRF2BPL leads to the partial presence of full-length IRF2BPL puncta in the cytoplasm.

(C) Schematic of Pits locus in Drosophila indicating the location of MiMIC element (MI02926). The original $Pits^{MiMIC}$ allele is in the reverse orientation and thus is non-mutagenic, resulting in homozygous viable flies, and serves as a control strain. On the contrary, the $Pits^{TG4}$ allele truncates endogenous Pits creating a strong loss-of-function allele that is homozygous lethal.[8]

(D) Relative ATP levels in $Pits^{MiMIC}$/+ or $Pits^{TG4}$/+ fly heads.

(E) Female flies that are heterozygous for the PitsTG4 allele display a slow, age-dependent climbing defect observed in older adults at 35 days after eclosion that are not observed at 25 days.

(F) $Pits^{MiMIC}$/+ or $Pits^{TG4}$/+ flies treated with CuATSM or DMSO as a control. CuATSM is at least partially neuroprotective in ameliorating climbing defects in $Pits^{TG4}$/+ flies at 35 days after eclosion. ANOVA followed by Tukey's LSD. p value (p), **p < 0.01, ***p < 0.001, ****p < 0.0001, ns = non-significant. Scale bar represents 2 μm.

including speed, the ability to bypass clonal isolation of single colonies or a pluripotent stem cell state, and retention of valuable epigenetic information.[21,41–43] This method has been used successfully in multiple laboratories studying various neurological disorders.[44–47] We chose to study the role of astrocytes in NEDAMSS as they often represent an overlooked but important source of disease pathogenesis. Astrocytes perform many roles to modulate development and neuronal activity including direct uptake and release of neurotransmitters, metabolism and regulation of metabolites, regulation of inflammation, establishment of brain structure, including the blood-brain barrier, and glial scarring in response to injury.[17,24,48–50] Some or all of these processes may be disrupted in neurological disease/trauma.[19] Astrocyte dysfunction has been shown to contribute to pathology in ALS, AD, PD, HD, tuberous sclerosis, Rett syndrome, and other autism spectrum and seizure disorders.[19,51]

Our four subjects with heterozygous nonsense mutations in *IRF2BPL* gene exhibited a progressive course of neurological regression. Patients P1, P2, and P3 demonstrated severe developmental disability and loss of motor skills, whereas the youngest patient, P4, had a mild form of developmental delay.[8–10] Our results show that most patient cell lines, with exception of the adult sample (P3), did not display the expected reduction in IRF2BPL protein expression that would be indicative of insufficient protein production from one allele (haploinsufficiency). Instead, we observed mislocalization of IRF2BPL protein that was highly prominent in NEDAMSS astrocytes leading to smears and aggregation in the cytoplasm. Aggregates of peptides or proteins are a major hallmark of many neurological diseases including ALS, frontotemporal dementia, AD, PD, HD, Creutzfeldt-Jacob's Disease, and spinal and bulbar muscular atrophy.[52,53] Intriguingly, the truncated protein in patient P4 includes the NLS unlike the mutated proteins from other patients. Similar to subject P4, mild autistic syndrome has been reported by another NEDAMSS patient (N701fs) that has the NLS preserved.[54] Thus, it is possible that the preservation of the NLS correlates with a milder form of the disease. However, while we saw differences in the amount of IRF2BPL in the nucleus and cytoplasm of healthy astrocytes transduced with the P4 mutant, we did not observe any difference when using the patients' original cells without overexpressing the mutant protein. Thus, further studies will be needed to evaluate the impact of an intact NLS on the patient phenotype and potential correlation to mislocalization pattern in the future.

In addition to the altered protein localization, astrocytes from NEDAMSS patients were non-supportive to cocultured neurons and showed an aberrant mitochondrial phenotype with increased network fractionation and mitochondrial respiration. Such an increase in oxidative phosphorylation indicates mitochondrial damage and inefficiency, which has been shown previously in AD neurons.[55] The disease phenotypes shown *in vitro* were ameliorated by the treatment of NEDAMSS astrocytes with a small molecule, CuATSM. Importantly, the findings from our *in vitro* assays were recapitulated in the fly model where we confirmed mislocalization of IRF2BPL via co-expression with the truncated form and age-dependent reduction in motor function, which was ameliorated by CuATSM treatment in a dominant model of truncated Pits (IRF2BPL ortholog) in flies.

Our data also show global transcriptional changes in patient iAs compared with healthy cell lines. Somatostatin receptor 2 (*SSTR2*) was highly downregulated in patient iAs. This G-protein-coupled receptor is involved in mitochondrial-mediated apoptosis and contributes to neuromodulatory effects in the cerebral cortex,[56] and its downregulation may contribute to aberrant phenotypes shown *in vitro* in patient iAs. Early growth response protein 2 (*ERG2*) dysregulation could lead to multiple phenotypes displayed by patient iAs as it has been proposed to play a role in dendritic complexity, cognition, and maintenance of mitochondrial membrane potential.[57] Moreover, defects in this gene are associated with Charcot-Marie-Tooth disease.[58,59] Similarly, upregulation of AKT serine/threonine kinase 3 and neuregulin-2 can be detrimental to mitochondrial function[60,61] or neuronal development,[62] respectively. In a recent collaborative report, we discovered that loss of IRF2BPL in NEDAMSS models in *Drosophila*, zebrafish, and patient iAs causes increased *WNT1* transcription.[14] Our RNA-seq data show that some WNT ligands (*WNT5A*, *WNT16*, *WNT9B*, and *WNT10B*) are also upregulated in NEDAMSS iAs (Table S2). Interestingly, increased Wnt signaling leads to increased mitochondrial biogenesis[63] as well as changes in mitochondrial morphology and dynamics.[64] Thus, altered Wnt signaling could in part underlie the increase in mitochondrial respiration and changes in mitochondrial dynamics in NEDAMSS iAs. Further studies are required to determine if loss of IRF2BPL activity as a transcriptional regulator directly causes differential expression of neurodevelopmental and metabolic genes or if both are interrelated in a different fashion.

CuATSM is a positron emission tomography imaging agent that can readily cross the blood-brain barrier.[26,65] The drug has a low reduction potential that facilitates selective release of copper in damaged cells.[31,65] Studies have shown that CuATSM exerts selective, neuroprotective effects in disease-affected regions of the CNS in ALS, PD, and mitochondrial encephalopathy, lactic acidosis, and stroke-like episodes syndrome.[26,30,65] Importantly, results from the phase I clinical trial showed that CuATSM could slow disease progression and improve the respiratory and cognitive function in ALS patients, but the mechanism of action is not fully understood.[66] Interestingly, treatment of NEDAMSS patient iAs with CuATSM significantly improved their supportive role for neurons in coculture assays and reduced the increased mitochondrial respiration in patients to normal rates. Upon investigating the mechanism of action of CuATSM, we found that the drug does not resolve the mislocalization of IRF2BPL protein in patient iAs, which might indicate that the aggregates are not mechanistically responsible for the lack of neuronal support or mitochondrial dysfunction. This is consistent with findings from the literature that protein aggregates might not necessarily be inherently toxic.[67] For example, recent evidence has indicated that in AD, soluble Aβ oligomers, rather than the insoluble aggregates, are the main neurotoxic species (reviewed in Zhou and Liu[68]). Interestingly, previous studies have reported that CuATSM significantly improved the survival and locomotor function in ALS-related $SOD1^{G37R}$ mouse model, without decreasing misfolded SOD1 aggregates.[26,30,31,65,69] In our study, the transcriptional profile of drug-treated NEDAMSS patient iAs shows upregulation of metal ion homeostasis pathways,

which is essential for cellular viability (Table S4). Hence, selective metal homeostasis could result in improved mitochondrial function in patient iAs, which in turn could lead to neuroprotection. Of note, patient P1 iAs did not show elevated mitochondrial respiration, but they showed elevated *WNT* transcription and still responded beneficially to CuATSM treatment. It is possible that this discrepancy could be due to the overall lower number of mitochondria in these cells, or alternatively, other pathways could be involved or act in combination to improve neuron viability. Furthermore, as the knockdown of IRF2BPL in healthy iAs resulted in neuronal loss in coculture assays similar to that observed with coculture of NEDAMSS patient lines, it is possible that the cellular phenotypes in NEDAMSS iAs likely stem from loss of IRF2BPL nuclear function rather than toxic gain of function from mislocalized or aggregated IRF2BPL. Further studies need to be conducted to shed light upon how loss/reduction of IRF2BPL impacts metal homeostasis or if abnormal Wnt signaling or other factors are responsible for the phenotypes.

Overall, we have generated an *in vitro* modeling system for NEDAMSS. Using this model, we discovered a cytoplasmic sequestration of full-length IRF2BPL due to its interaction with mutant truncated IRF2BPL in NEDAMSS astrocytes. We report cellular phenotypes including failure of NEDAMSS astrocytes to support neuron growth and survival and aberrant cellular metabolism that could be attributed to the loss of IRF2BPL function. Our data also show that gene expression changes and therapeutic response associated with these phenotypes demonstrate both a disease-specific and mutation-specific pattern, potentially indicating multiple mechanisms of NEDAMSS pathogenicity. Finally, we have identified CuATSM as a promising therapeutic that may be able to slow or halt the progression of NEDAMSS. Future research is required to understand the role of IRF2BPL in causing mitochondrial dysfunction in patients. This would be of particular interest as mitochondrial dysfunction/aberrant cellular metabolism is emerging as an increasingly important factor in many neurological/seizure disorders.[70] Therefore, improvement of mitochondrial function/health could become a potential therapeutic strategy with implications across a wide spectrum of disorders.

Limitations of the study

Unlike other patient lines, only the adult subject (P3) showed a significant loss of IRF2BPL protein. Additional adult patient cell lines need to be investigated to determine if age-dependent loss of IRF2BPL takes place in patients. The cytoplasmic sequestration of full-length IRF2BPL was observed in cases of NEDAMSS with nonsense mutations, and it remains unclear whether cytoplasmic sequestration occurs in cells derived from individuals with missense variants or other mutations preserving the NLS.

STAR★METHODS

Detailed methods are provided in the online version of this paper and include the following:

- KEY RESOURCES TABLE
- RESOURCE AVAILABILITY
  - Lead contact
  - Materials availability
  - Data and code availability
- EXPERIMENTAL MODEL AND SUBJECT DETAILS
  - Skin fibroblasts
  - *In vivo* studies in Drosophila
- METHOD DETAILS
  - Direct conversion of fibroblasts to neurons
  - Reprogramming of fibroblasts to astrocytes
  - Immunofluorescence
  - Western blot
  - mRNA SNP-genotyping
  - HA pull-down assay and lentivirus transduction
  - Coculture assay
  - Computational analysis of mitochondria
  - Seahorse ATP real-time rate assay
  - RNA-seq analysis
- QUANTIFICATION AND STATISTICAL ANALYSIS

SUPPLEMENTAL INFORMATION

Supplemental information can be found online at https://doi.org/10.1016/j.celrep.2022.111751.

ACKNOWLEDGMENTS

The authors thank the California Center for Rare Diseases at UCLA for provision of primary patient cultures. We specially would like to thank the Families of SCN2A Foundation for sponsoring the Seahorse equipment. We are indebted to Dr. Joe Beckman for gifting us the CuATSM drug that was used in our study. We also would like to acknowledge Annalisa Hartlaub for her immense support in laboratory organization, sorting of neurons for coculture assays, and image quantification. This work was primarily supported by the Stand by Eli foundation (www.standbyeli.org) via The Giving Back Fund (www.givingback.org). Research reported in this publication was also supported by the Eunice Kennedy Shriver National Institute of Child Health & Human Development of the National Institutes of Health under Award Number P50HD103555 for use of the Neurovisualization core facilities at BCM. P.L. was supported by National Spectrum Consortium to Poland, NCN OPUS Grant No. 2017/27/B/NZ1/02401.

AUTHOR CONTRIBUTIONS

Conceptualization, S.S.R., C.D.R., S.L., and K.C.M.; investigation, S.S.R., D.D., P.C.M., S.P., F.R., P.L., P.G., P.B., X.Z., J.R.C., and M.B.; resources, K.C.M., N.W., and H.J.B.; writing – original draft, S.S.R., S.L., C.D.R., S.P., P.C.M., D.D., and K.C.M.; writing – review & editing, S.S.R., P.C.M., D.D., S.L., S.P., C.D.R., J.R.C., F.R., P.B., P.L., P.G., M.B., X.J., N.W., H.J.B., and K.C.M.; supervision, M.B., N.W., H.J.B., and K.C.M.; funding acquisition, H.J.B. and K.C.M.

DECLARATION OF INTERESTS

The authors declare no competing interests.

INCLUSION AND DIVERSITY

We support inclusive, diverse, and equitable conduct of research.

Received: May 25, 2022
Revised: September 23, 2022
Accepted: November 8, 2022
Published: December 6, 2022

REFERENCES

1. Rampazzo, A., Pivotto, F., Occhi, G., Tiso, N., Bortoluzzi, S., Rowen, L., Hood, L., Nava, A., and Danieli, G.A. (2000). Characterization of C14orf4, a novel intronless human gene containing a polyglutamine repeat, mapped to the ARVD1 critical region. Biochem. Biophys. Res. Commun. *278*, 766–774. https://doi.org/10.1006/bbrc.2000.3883.
2. Heger, S., Mastronardi, C., Dissen, G.A., Lomniczi, A., Cabrera, R., Roth, C.L., Jung, H., Galimi, F., Sippell, W., and Ojeda, S.R. (2007). Enhanced at puberty 1 (EAP1) is a new transcriptional regulator of the female neuroendocrine reproductive axis. J. Clin. Invest. *117*, 2145–2154. https://doi.org/10.1172/JCI31752.
3. Mueller, J.K., Koch, I., Lomniczi, A., Loche, A., Rulfs, T., Castellano, J.M., Kiess, W., Ojeda, S., and Heger, S. (2012). Transcription of the human EAP1 gene is regulated by upstream components of a puberty-controlling Tumor Suppressor Gene network. Mol. Cell. Endocrinol. *351*, 184–198. https://doi.org/10.1016/j.mce.2011.12.004.
4. Dissen, G.A., Lomniczi, A., Heger, S., Neff, T.L., and Ojeda, S.R. (2012). Hypothalamic EAP1 (enhanced at puberty 1) is required for menstrual cyclicity in nonhuman primates. Endocrinology *153*, 350–361. https://doi.org/10.1210/en.2011-1541.
5. Mancini, A., Howard, S.R., Cabrera, C.P., Barnes, M.R., David, A., Wehkalampi, K., Heger, S., Lomniczi, A., Guasti, L., Ojeda, S.R., and Dunkel, L. (2019). EAP1 regulation of GnRH promoter activity is important for human pubertal timing. Hum. Mol. Genet. *28*, 1357–1368. https://doi.org/10.1093/hmg/ddy451.
6. Xu, J., and Li, P. (2016). Expression of EAP1 and CUX1 in the hypothalamus of female rats and relationship with KISS1 and GnRH. Endocr. J. *63*, 681–690. https://doi.org/10.1507/endocrj.EJ16-0123.
7. Higashimori, A., Dong, Y., Zhang, Y., Kang, W., Nakatsu, G., Ng, S.S.M., Arakawa, T., Sung, J.J.Y., Chan, F.K.L., and Yu, J. (2018). Forkhead box F2 suppresses gastric cancer through a novel FOXF2-IRF2BPL-beta-catenin signaling Axis. Cancer Res. *78*, 1643–1656. https://doi.org/10.1158/0008-5472.CAN-17-2403.
8. Marcogliese, P.C., Shashi, V., Spillmann, R.C., Stong, N., Rosenfeld, J.A., Koenig, M.K., Martínez-Agosto, J.A., Herzog, M., Chen, A.H., Dickson, P.I., et al. (2018). IRF2BPL is associated with neurological phenotypes. Am. J. Hum. Genet. *103*, 245–260. https://doi.org/10.1016/j.ajhg.2018.07.006.
9. Tran Mau-Them, F., Guibaud, L., Duplomb, L., Keren, B., Lindstrom, K., Marey, I., Mochel, F., van den Boogaard, M.J., Oegema, R., Nava, C., et al. (2019). De novo truncating variants in the intronless IRF2BPL are responsible for developmental epileptic encephalopathy. Genet. Med. *21*, 1008–1014. https://doi.org/10.1038/s41436-018-0143-0.
10. Shelkowitz, E., Singh, J.K., Larson, A., and Elias, E.R. (2019). IRF2BPL gene mutation: expanding on neurologic phenotypes. Am. J. Med. Genet. *179*, 2263–2271. https://doi.org/10.1002/ajmg.a.61328.
11. Ganos, C., Zittel, S., Hidding, U., Funke, C., Biskup, S., and Bhatia, K.P. (2019). IRF2BPL mutations cause autosomal dominant dystonia with anarthria, slow saccades and seizures. Parkinsonism Relat. Disord. *68*, 57–59. https://doi.org/10.1016/j.parkreldis.2019.09.020.
12. Qian, X.H., Liu, X.Y., Zhu, Z.Y., Wang, S.G., Song, X.X., Chen, G., Wu, J.Y., Tang, H.D., and Cao, L. (2021). Neurodevelopmental disorder caused by a truncating de novo variant of IRF2BPL. Seizure *84*, 47–52. https://doi.org/10.1016/j.seizure.2020.11.006.
13. Vinkšel, M., Writzl, K., Maver, A., and Peterlin, B. (2021). Improving diagnostics of rare genetic diseases with NGS approaches. J. Community Genet. *12*, 247–256. https://doi.org/10.1007/s12687-020-00500-5.
14. Marcogliese, P.C., Dutta, D., Ray, S.S., Dang, N.D.P., Zuo, Z., Wang, Y., Lu, D., Fazal, F., Ravenscroft, T.A., Chung, H., et al. (2022). Loss of IRF2BPL impairs neuronal maintenance through excess Wnt signaling. Sci. Adv. *8*, eabl5613. https://doi.org/10.1126/sciadv.abl5613.
15. Hu, W., Qiu, B., Guan, W., Wang, Q., Wang, M., Li, W., Gao, L., Shen, L., Huang, Y., Xie, G., et al. (2015). Direct conversion of normal and Alzheimer's disease human fibroblasts into neuronal cells by small molecules. Cell Stem Cell *17*, 204–212. https://doi.org/10.1016/j.stem.2015.07.006.
16. Meyer, K., Ferraiuolo, L., Miranda, C.J., Likhite, S., McElroy, S., Renusch, S., Ditsworth, D., Lagier-Tourenne, C., Smith, R.A., Ravits, J., et al. (2014). Direct conversion of patient fibroblasts demonstrates non-cell autonomous toxicity of astrocytes to motor neurons in familial and sporadic ALS. Proc. Natl. Acad. Sci. USA *111*, 829–832. https://doi.org/10.1073/pnas.1314085111.
17. Chaboub, L.S., and Deneen, B. (2013). Astrocyte form and function in the developing central nervous system. Semin. Pediatr. Neurol. *20*, 230–235. https://doi.org/10.1016/j.spen.2013.10.003.
18. Blackburn, D., Sargsyan, S., Monk, P.N., and Shaw, P.J. (2009). Astrocyte function and role in motor neuron disease: a future therapeutic target? Glia *57*, 1251–1264. https://doi.org/10.1002/glia.20848.
19. Phatnani, H., and Maniatis, T. (2015). Astrocytes in neurodegenerative disease. Cold Spring Harb. Perspect. Biol. *7*, a020628. https://doi.org/10.1101/cshperspect.a020628.
20. Dennys, C.N., Sierra-Delgado, J.A., Ray, S.S., Hartlaub, A.M., Roussel, F.S., Rodriguez, Y., and Meyer, K. (2021). In vitro modeling for neurological diseases using direct conversion from fibroblasts to neuronal progenitor cells and differentiation into astrocytes. J. Vis. Exp. https://doi.org/10.3791/62016.
21. Gatto, N., Dos Santos Souza, C., Shaw, A.C., Bell, S.M., Myszczynska, M.A., Powers, S., Meyer, K., Castelli, L.M., Karyka, E., Mortiboys, H., et al. (2021). Directly converted astrocytes retain the ageing features of the donor fibroblasts and elucidate the astrocytic contribution to human CNS health and disease. Aging Cell *20*, e13281. https://doi.org/10.1111/acel.13281.
22. Pekny, M., and Pekna, M. (2014). Astrocyte reactivity and reactive astrogliosis: costs and benefits. Physiol. Rev. *94*, 1077–1098. https://doi.org/10.1152/physrev.00041.2013.
23. Yeung, K.T., Das, S., Zhang, J., Lomniczi, A., Ojeda, S.R., Xu, C.F., Neubert, T.A., and Samuels, H.H. (2011). A novel transcription complex that selectively modulates apoptosis of breast cancer cells through regulation of FASTKD2. Mol. Cell Biol. *31*, 2287–2298. https://doi.org/10.1128/MCB.01381-10.
24. Bélanger, M., and Magistretti, P.J. (2009). The role of astroglia in neuroprotection. Dialogues Clin. Neurosci. *11*, 281–295.
25. Dennys, C.N., Roussel, F., Rodrigo, R., Zhang, X., Sierra Delgado, A., Hartlaub, A., Saelim-Ector, A., Ray, W., Heintzman, S., Fox, A., et al. (2022). CuATSM effectively ameliorates ALS patient astrocyte-mediated motor neuron toxicity in human in vitro models of amyotrophic lateral sclerosis. Glia. https://doi.org/10.1002/glia.24278.
26. Nikseresht, S., Hilton, J.B.W., Kysenius, K., Liddell, J.R., and Crouch, P.J. (2020). Copper-ATSM as a treatment for ALS: support from mutant SOD1 models and beyond. Life *10*, E271. https://doi.org/10.3390/life10110271.
27. NCT04082832. https://clinicaltrials.gov/ct2/show/NCT04082832.
28. NCT03204929. https://clinicaltrials.gov/ct2/show/NCT03204929.
29. Wang, Y., Xu, E., Musich, P.R., and Lin, F. (2019). Mitochondrial dysfunction in neurodegenerative diseases and the potential countermeasure. CNS Neurosci. Ther. *25*, 816–824. https://doi.org/10.1111/cns.13116.
30. Kuo, M.T.H., Beckman, J.S., and Shaw, C.A. (2019). Neuroprotective effect of CuATSM on neurotoxin-induced motor neuron loss in an ALS mouse model. Neurobiol. Dis. *130*, 104495. https://doi.org/10.1016/j.nbd.2019.104495.
31. Hung, L.W., Villemagne, V.L., Cheng, L., Sherratt, N.A., Ayton, S., White, A.R., Crouch, P.J., Lim, S., Leong, S.L., Wilkins, S., et al. (2012). The hypoxia imaging agent CuII(atsm) is neuroprotective and improves motor and cognitive functions in multiple animal models of Parkinson's disease. J. Exp. Med. *209*, 837–854. https://doi.org/10.1084/jem.20112285.
32. Li, Y., Park, J.S., Deng, J.H., and Bai, Y. (2006). Cytochrome c oxidase subunit IV is essential for assembly and respiratory function of the enzyme

complex. J. Bioenerg. Biomembr. *38*, 283–291. https://doi.org/10.1007/s10863-006-9052-z.

33. Song, W., Song, Y., Kincaid, B., Bossy, B., and Bossy-Wetzel, E. (2013). Mutant SOD1G93A triggers mitochondrial fragmentation in spinal cord motor neurons: neuroprotection by SIRT3 and PGC-1alpha. Neurobiol. Dis. *51*, 72–81. https://doi.org/10.1016/j.nbd.2012.07.004.

34. Yang, D., Ying, J., Wang, X., Zhao, T., Yoon, S., Fang, Y., Zheng, Q., Liu, X., Yu, W., and Hua, F. (2021). Mitochondrial dynamics: a key role in neurodegeneration and a potential target for neurodegenerative disease. Front. Neurosci. *15*, 654785. https://doi.org/10.3389/fnins.2021.654785.

35. Brand, A.H., and Perrimon, N. (1993). Targeted gene expression as a means of altering cell fates and generating dominant phenotypes. Development *118*, 401–415.

36. Diao, F., Ironfield, H., Luan, H., Diao, F., Shropshire, W.C., Ewer, J., Marr, E., Potter, C.J., Landgraf, M., and White, B.H. (2015). Plug-and-play genetic access to drosophila cell types using exchangeable exon cassettes. Cell Rep. *10*, 1410–1421. https://doi.org/10.1016/j.celrep.2015.01.059.

37. Lee, P.T., Zirin, J., Kanca, O., Lin, W.W., Schulze, K.L., Li-Kroeger, D., Tao, R., Devereaux, C., Hu, Y., Chung, V., et al. (2018). A gene-specific T2A-GAL4 library for Drosophila. Elife *7*, e35574. https://doi.org/10.7554/eLife.35574.

38. Venken, K.J.T., Schulze, K.L., Haelterman, N.A., Pan, H., He, Y., Evans-Holm, M., Carlson, J.W., Levis, R.W., Spradling, A.C., Hoskins, R.A., and Bellen, H.J. (2011). MiMIC: a highly versatile transposon insertion resource for engineering Drosophila melanogaster genes. Nat. Methods *8*, 737–743. https://doi.org/10.1038/nmeth.1662.

39. Ginevrino, M., Battini, R., Nuovo, S., Simonati, A., Micalizzi, A., Contaldo, I., Serpieri, V., and Valente, E.M. (2020). A novel IRF2BPL truncating variant is associated with endolysosomal storage. Mol. Biol. Rep. *47*, 711–714. https://doi.org/10.1007/s11033-019-05109-7.

40. Prilop, L., Buchert, R., Woerz, S., Gerloff, C., Haack, T.B., and Zittel, S. (2020). IRF2BPL mutation causes nigrostriatal degeneration presenting with dystonia, spasticity and keratoconus. Parkinsonism Relat. Disord. *79*, 141–143. https://doi.org/10.1016/j.parkreldis.2020.03.030.

41. Ladewig, J., Koch, P., and Brüstle, O. (2013). Leveling Waddington: the emergence of direct programming and the loss of cell fate hierarchies. Nat. Rev. Mol. Cell Biol. *14*, 225–236.

42. Kelaini, S., Cochrane, A., and Margariti, A. (2014). Direct reprogramming of adult cells: avoiding the pluripotent state. Stem Cells Cloning. *7*, 19–29. https://doi.org/10.2147/SCCAA.S38006.

43. Stricker, S.H., and Götz, M. (2021). Epigenetic regulation of neural lineage elaboration: implications for therapeutic reprogramming. Neurobiol. Dis. *148*, 105174. https://doi.org/10.1016/j.nbd.2020.105174.

44. Boczonadi, V., Meyer, K., Gonczarowska-Jorge, H., Griffin, H., Roos, A., Bartsakoulia, M., Bansagi, B., Ricci, G., Palinkas, F., Zahedi, R.P., et al. (2018). Mutations in glycyl-tRNA synthetase impair mitochondrial metabolism in neurons. Hum. Mol. Genet. *27*, 2187–2204. https://doi.org/10.1093/hmg/ddy127.

45. Hautbergue, G.M., Castelli, L.M., Ferraiuolo, L., Sanchez-Martinez, A., Cooper-Knock, J., Higginbottom, A., Lin, Y.H., Bauer, C.S., Dodd, J.E., Myszczynska, M.A., et al. (2017). SRSF1-dependent nuclear export inhibition of C9ORF72 repeat transcripts prevents neurodegeneration and associated motor deficits. Nat. Commun. *8*, 16063. https://doi.org/10.1038/ncomms16063.

46. Webster, C.P., Smith, E.F., Bauer, C.S., Moller, A., Hautbergue, G.M., Ferraiuolo, L., Myszczynska, M.A., Higginbottom, A., Walsh, M.J., Whitworth, A.J., et al. (2016). The C9orf72 protein interacts with Rab1a and the ULK1 complex to regulate initiation of autophagy. EMBO J. *35*, 1656–1676. https://doi.org/10.15252/embj.201694401.

47. Meyer, S., Wörsdörfer, P., Günther, K., Thier, M., and Edenhofer, F. (2015). Derivation of adult human fibroblasts and their direct conversion into expandable neural progenitor cells. J. Vis. Exp., e52831. https://doi.org/10.3791/52831.

48. Müller, H.W., Junghans, U., and Kappler, J. (1995). Astroglial neurotrophic and neurite-promoting factors. Pharmacol. Ther. *65*, 1–18. https://doi.org/10.1016/0163-7258(94)00047-7.

49. Verhoog, Q.P., Holtman, L., Aronica, E., and van Vliet, E.A. (2020). Astrocytes as guardians of neuronal excitability: mechanisms underlying epileptogenesis. Front. Neurol. *11*, 591690. https://doi.org/10.3389/fneur.2020.591690.

50. Cekanaviciute, E., and Buckwalter, M.S. (2016). Astrocytes: integrative regulators of neuroinflammation in Stroke and other neurological diseases. Neurotherapeutics *13*, 685–701. https://doi.org/10.1007/s13311-016-0477-8.

51. McGann, J.C., Lioy, D.T., and Mandel, G. (2012). Astrocytes conspire with neurons during progression of neurological disease. Curr. Opin. Neurobiol. *22*, 850–858. https://doi.org/10.1016/j.conb.2012.03.009.

52. Corsaro, A., Thellung, S., Villa, V., Nizzari, M., and Florio, T. (2012). Role of prion protein aggregation in neurotoxicity. Int. J. Mol. Sci. *13*, 8648–8669. https://doi.org/10.3390/ijms13078648.

53. Monaco, A., and Fraldi, A. (2020). Protein aggregation and dysfunction of autophagy-lysosomal pathway: a vicious cycle in lysosomal storage diseases. Front. Mol. Neurosci. *13*, 37. https://doi.org/10.3389/fnmol.2020.00037.

54. Iossifov, I., O'Roak, B.J., Sanders, S.J., Ronemus, M., Krumm, N., Levy, D., Stessman, H.A., Witherspoon, K.T., Vives, L., Patterson, K.E., et al. (2014). The contribution of de novo coding mutations to autism spectrum disorder. Nature *515*, 216–221. https://doi.org/10.1038/nature13908.

55. Sonntag, K.C., Ryu, W.I., Amirault, K.M., Healy, R.A., Siegel, A.J., McPhie, D.L., Forester, B., and Cohen, B.M. (2017). Late-onset Alzheimer's disease is associated with inherent changes in bioenergetics profiles. Sci. Rep. *7*, 14038. https://doi.org/10.1038/s41598-017-14420-x.

56. Stumm, R.K., Zhou, C., Schulz, S., Endres, M., Kronenberg, G., Allen, J.P., Tulipano, G., and Höllt, V. (2004). Somatostatin receptor 2 is activated in cortical neurons and contributes to neurodegeneration after focal ischemia. J. Neurosci. *24*, 11404–11415. https://doi.org/10.1523/JNEUROSCI.3834-04.2004.

57. Piao Zhang, Y.C., Zhang, S., Fang, M., Lin, X., Liu, T., Zhou, Y., Yu, X., and Chen, G. (2020). Egr2 Upregulation Induced Mitochondrial IronOverload Implicating in Cognitive Deficits after Sevoflurane Administration. Pre-print from Research Square. https://doi.org/10.21203/rs.3.rs-104467/v1.

58. Blanco-Cantó, M.E., Patel, N., Velasco-Aviles, S., Casillas-Bajo, A., Salas-Felipe, J., García-Escrivá, A., Díaz-Marín, C., and Cabedo, H. (2020). Novel EGR2 variant that associates with Charcot-Marie-Tooth disease when combined with lipopolysaccharide-induced TNF-alpha factor T49M polymorphism. Neurol. Genet. *6*, e407. https://doi.org/10.1212/NXG.0000000000000407.

59. Sevilla, T., Sivera, R., Martínez-Rubio, D., Lupo, V., Chumillas, M.J., Calpena, E., Dopazo, J., Vílchez, J.J., Palau, F., and Espinós, C. (2015). The EGR2 gene is involved in axonal Charcot-Marie-Tooth disease. Eur. J. Neurol. *22*, 1548–1555. https://doi.org/10.1111/ene.12782.

60. Cohen, M.M., Jr. (2013). The AKT genes and their roles in various disorders. Am. J. Med. Genet. *161A*, 2931–2937. https://doi.org/10.1002/ajmg.a.36101.

61. Polytarchou, C., Hatziapostolou, M., Yau, T.O., Christodoulou, N., Hinds, P.W., Kottakis, F., Sanidas, I., and Tsichlis, P.N. (2020). Akt3 induces oxidative stress and DNA damage by activating the NADPH oxidase via phosphorylation of p47(phox). Proc. Natl. Acad. Sci. USA *117*, 28806–28815. https://doi.org/10.1073/pnas.2017830117.

62. Longart, M., Liu, Y., Karavanova, I., and Buonanno, A. (2004). Neuregulin-2 is developmentally regulated and targeted to dendrites of central neurons. J. Comp. Neurol. *472*, 156–172. https://doi.org/10.1002/cne.20016.

63. Yoon, J.C., Ng, A., Kim, B.H., Bianco, A., Xavier, R.J., and Elledge, S.J. (2010). Wnt signaling regulates mitochondrial physiology and insulin sensitivity. Genes Dev. *24*, 1507–1518. https://doi.org/10.1101/gad.1924910.

64. Godoy, J.A., Arrázola, M.S., Ordenes, D., Silva-Alvarez, C., Braidy, N., and Inestrosa, N.C. (2014). Wnt-5a ligand modulates mitochondrial fission-fusion in rat hippocampal neurons. J. Biol. Chem. *289*, 36179–36193. https://doi.org/10.1074/jbc.M114.557009.

65. Soon, C.P.W., Donnelly, P.S., Turner, B.J., Hung, L.W., Crouch, P.J., Sherratt, N.A., Tan, J.L., Lim, N.K.H., Lam, L., Bica, L., et al. (2011). Diacetyl-bis(N(4)-methylthiosemicarbazonato) copper(II) (CuII(atsm)) protects against peroxynitrite-induced nitrosative damage and prolongs survival in amyotrophic lateral sclerosis mouse model. J. Biol. Chem. *286*, 44035–44044. https://doi.org/10.1074/jbc.M111.274407.

66. Carvalho, J.. CuATSM Therapy May Slow ALS Progression, Improving Cognition and Respiration in Patients, Phase 1 Trial Shows. https://alsnewstoday.com/news/cuatsm-may-slow-als-progression-improve-cognition-respiration-phase-1-trial/.

67. Jochum, T., Ritz, M.E., Schuster, C., Funderburk, S.F., Jehle, K., Schmitz, K., Brinkmann, F., Hirtz, M., Moss, D., and Cato, A.C.B. (2012). Toxic and non-toxic aggregates from the SBMA and normal forms of androgen receptor have distinct oligomeric structures. Biochim. Biophys. Acta *1822*, 1070–1078. https://doi.org/10.1016/j.bbadis.2012.02.006.

68. Zhou, J., and Liu, B. (2013). Alzheimer's disease and prion protein. Intractable Rare Dis. Res. *2*, 35–44. https://doi.org/10.5582/irdr.2013.v2.2.35.

69. Gros-Louis, F., Soucy, G., Larivière, R., and Julien, J.P. (2010). Intracerebroventricular infusion of monoclonal antibody or its derived Fab fragment against misfolded forms of SOD1 mutant delays mortality in a mouse model of ALS. J. Neurochem. *113*, 1188–1199. https://doi.org/10.1111/j.1471-4159.2010.06683.x.

70. Norat, P., Soldozy, S., Sokolowski, J.D., Gorick, C.M., Kumar, J.S., Chae, Y., Yağmurlu, K., Prada, F., Walker, M., Levitt, M.R., et al. (2020). Mitochondrial dysfunction in neurological disorders: exploring mitochondrial transplantation. NPJ Regen. Med. *5*, 22. https://doi.org/10.1038/s41536-020-00107-x.

71. Calleja, M., Herranz, H., Estella, C., Casal, J., Lawrence, P., Simpson, P., and Morata, G. (2000). Generation of medial and lateral dorsal body domains by the pannier gene of Drosophila. Development *127*, 3971–3980.

72. Chung, H.L., Mao, X., Wang, H., Park, Y.J., Marcogliese, P.C., Rosenfeld, J.A., Burrage, L.C., Liu, P., Murdock, D.R., Yamamoto, S., et al. (2020). De novo variants in CDK19 are associated with a syndrome involving intellectual disability and epileptic encephalopathy. Am. J. Hum. Genet. *106*, 717–725. https://doi.org/10.1016/j.ajhg.2020.04.001.

73. Bischof, J., Maeda, R.K., Hediger, M., Karch, F., and Basler, K. (2007). An optimized transgenesis system for Drosophila using germ-line-specific phiC31 integrases. Proc. Natl. Acad. Sci. USA *104*, 3312–3317. https://doi.org/10.1073/pnas.0611511104.

74. Venken, K.J.T., He, Y., Hoskins, R.A., and Bellen, H.J. (2006). P[acman]: a BAC transgenic platform for targeted insertion of large DNA fragments in D. melanogaster. Science *314*, 1747–1751. https://doi.org/10.1126/science.1134426.

75. Schindelin, J., Arganda-Carreras, I., Frise, E., Kaynig, V., Longair, M., Pietzsch, T., Preibisch, S., Rueden, C., Saalfeld, S., Schmid, B., et al. (2012). Fiji: an open-source platform for biological-image analysis. Nat. Methods *9*, 676–682. https://doi.org/10.1038/nmeth.2019.

76. Rio, D.C., Ares, M., Jr., Hannon, G.J., and Nilsen, T.W. (2010). Purification of RNA using TRIzol (TRI reagent). Cold Spring Harb. Protoc. *2010*, pdb prot5439. https://doi.org/10.1101/pdb.prot5439.

77. Kingston, R.E., Chen, C.A., and Rose, J.K. (2003). Calcium phosphate transfection. Curr. Protoc. Mol. Biol.mb0901s63 Chapter 9, Unit 9 1. https://doi.org/10.1002/0471142727.

78. Tiscornia, G., Singer, O., and Verma, I.M. (2006). Production and purification of lentiviral vectors. Nat. Protoc. *1*, 241–245. https://doi.org/10.1038/nprot.2006.37.

79. Dobin, A., Davis, C.A., Schlesinger, F., Drenkow, J., Zaleski, C., Jha, S., Batut, P., Chaisson, M., and Gingeras, T.R. (2013). STAR: ultrafast universal RNA-seq aligner. Bioinformatics *29*, 15–21. https://doi.org/10.1093/bioinformatics/bts635.

80. Anders, S., Pyl, P.T., and Huber, W. (2015). HTSeq–a Python framework to work with high-throughput sequencing data. Bioinformatics *31*, 166–169. https://doi.org/10.1093/bioinformatics/btu638.

81. Frankish, A., Diekhans, M., Ferreira, A.M., Johnson, R., Jungreis, I., Loveland, J., Mudge, J.M., Sisu, C., Wright, J., Armstrong, J., et al. (2019). GENCODE reference annotation for the human and mouse genomes. Nucleic Acids Res. *47*, D766–D773. https://doi.org/10.1093/nar/gky955.

82. Love, M.I., Huber, W., and Anders, S. (2014). Moderated estimation of fold change and dispersion for RNA-seq data with DESeq2. Genome Biol. *15*, 550. https://doi.org/10.1186/s13059-014-0550-8.

83. Kolde, R. (2019). Pheatmap: Pretty Heatmaps. R Package version 1.0.12. .

84. Chung, H.L., Augustine, G.J., and Choi, K.W. (2016). Drosophila Schip1 links expanded and tao-1 to regulate hippo signaling. Dev. Cell *36*, 511–524. https://doi.org/10.1016/j.devcel.2016.02.004.

85. Yoon, W.H., Sandoval, H., Nagarkar-Jaiswal, S., Jaiswal, M., Yamamoto, S., Haelterman, N.A., Putluri, N., Putluri, V., Sreekumar, A., Tos, T., et al. (2017). Loss of Nardilysin, a mitochondrial Co-chaperone for alpha-Ketoglutarate Dehydrogenase, promotes mTORC1 activation and neurodegeneration. Neuron *93*, 115–131. https://doi.org/10.1016/j.neuron.2016.11.038.

STAR★METHODS

KEY RESOURCES TABLE

REAGENT or RESOURCE	SOURCE	IDENTIFIER
Antibodies		
IRF2BPL	Abcam	ab221099; RRID:AB_2684481
IRF2BPL	Novus Biologics	NBP2-14712; RRID:AB_2681258
Tuj1	Biolegend	801213; RRID:AB_2728521
Map2	Novus Biologics	NB300-213; RRID:AB_2138178
H3	Cell Signaling	3638; RRID:AB_1642229
HA	Cell Signaling	2367; RRID:AB_10691311
COXIV	Cell Signaling	4850; RRID:AB_2085424
ATP5a	Abcam	ab14748; RRID:AB_301447
Oligonucleotides		
Primer used for mutagenesis, see Table S5	This paper	N/A
Primers used for quantitative PCR, see Table S6	This paper	N/A
Recombinant DNA		
pcDNA3.1+CMV-N-HA-IRF2BPL	Genscript	N/A
pcDNA3.1+CMV-N-HA-P1	This paper	N/A
pcDNA3.1+CMV-N-HA-P2	This paper	N/A
pcDNA3.1+CMV-N-HA-P3	This paper	N/A
pcDNA3.1+CMV-N-HA-P4	This paper	N/A
LV-CMV-IRF2BPL	This paper	N/A
LV-pBOB-GFP	Addgene	12,337
LV-H2B-RFP	Addgene	26,001
LV-sh29	This paper	N/A
LV-CMV-P1	This paper	N/A
LV-CMV-P2	This paper	N/A
LV-CMV-P3	This paper	N/A
LV-CMV-P4	This paper	N/A
Deposited data		
RNA-seq dataset	NCBI GEO	GSE189909

RESOURCE AVAILABILITY

Lead contact

Further information and requests for resources and reagents should be directed to and will be fulfilled by the lead contact, Dr. Kathrin Meyer (kathrin.meyer@nationwidechildrens.org).

Materials availability

All requests for resources and reagents should be directed to the lead contact author. All reagents, which includes antibodies, proteins, plasmids, and virus, will be made available on request after completion of a Materials Transfer Agreement for non-commercial usage.

Data and code availability

All data reported in this paper will be shared by the lead contact upon request. RNA-seq data have been deposited at GEO and are publicly available as of the date of publication. The accession number is listed in the key resources table. This paper does not report original code. Any additional information required to reanalyze the data reported in this paper is available from the lead contact upon request.

EXPERIMENTAL MODEL AND SUBJECT DETAILS

Skin fibroblasts

Human skin fibroblasts (Table S1) were obtained from University of California, Los Angeles and Duke University, Durham. Informed consent was obtained from all subjects before sample collection. Receipt of human samples was granted through Nationwide Children's Hospital Institutional Review Board. The nonsense mutation present in each patient (P1, P2, P3 and P4) was confirmed by amplicon sequencing using the Illumina Hiseq 2000.

In vivo studies in Drosophila

The following fly stocks were generated previously: *nubbin-GAL4* (*w** *(P{GawB}nubbin-AC-62)*[71]; *UAS-IRF2BPL* (*y*^{1} *w***; PBac{UAS-hIRF2BPL.B}VK00037*) BDSC_78509[8]; UAS-LacZ (*w***; P{w[+mC] = UAS-lacZ.Exel}2*) BDSC_8529; Repo-GAL4 (*w*^{1118}*; P{GAL4}repo/TM3, Sb1*) BDSC_7415; *Pits*^{MiMIC} (*y*^{1} *w** *Mi*^{39}*Pits*^{MI02926}) BDSC_36165 ^{38}; *Pits*^{TG4} (*y*^{1} *w** *Mi{Trojan-GAL4.1}Pits*$^{MI02926\text{-}TG4.1}$*/FM7c*) BDSC_77731.[8]

UAS-IRF2BPL^{E172X}*::HA* flies were generated as previously described.[72] Briefly, site-directed mutagenesis was performed with the Q5 site-directed mutagenesis kit (NEB) on the IRF2BPL clone in the pDONR223 entry vector.[8] Primers listed in Table S5 were used to obtain *IRF2BPL*^{E172X}*::HA (P1:HA)* followed by Sanger verification. Using Gateway cloning (Thermo Fisher Scientific), the *P1::HA* cDNA entry clone in the pDONR223 vector was shuttled to the pUASg-attB-HA.[73] The construct was inserted into the VK37 (PBac{y[+]-attP}VK00037) docking site by φC31 mediated transgenesis.[74]

METHOD DETAILS

Direct conversion of fibroblasts to neurons

Patient and healthy fibroblasts were directly converted to neurons using small molecules as described previously with few modifications.[15] Briefly, 24-well plates with cover slips or 10 cm plates were coated with poly-D-lysine (50 μg/mL, Sigma) in borate buffer for an hour at room temperature. Next the plates were washed with Dulbecco's phosphate buffered saline (DPBS) (Gibco) and coated with laminin (10 μg/mL) in DMEM/F12 (Gibco) at 37°C for 2 h. Fibroblast cells at a density of 25,000 for a 24 well and 800,000 for a 10 cm plate were seeded with fibroblast culture medium for 1 day. The next day the cells were transferred into neuronal induction medium (DMEM/F12: Neurobasal [1:1] (Gibco) with 0.5% N-2 (Gibco), 1% B-27 (Gibco), cAMP (100 μM, Sigma), and bFGF-2 (20 ng/mL, Peprotech) with the following chemicals: VPA (0.5 mM, Sigma), CHIR99021 (3 μM, Axon medchem), repsox (1 μM, Biovision), forskolin (10 μM, Tocris), SP600125 (10 μM, Sigma), GO6983 (5 μM, Sigma) and Y-27632 (5 μM, Sigma). Half of the medium containing the chemicals was changed after 3 days with fresh induction medium. On the fifth day, cells were switched to neuronal maturation medium (DMEM/F12: Neurobasal [1:1] with 0.5% N-2, 1% B-27, cAMP (100 μM), bFGF-2 (20 ng/mL), BDNF (20 ng/mL, Peprotech) and GDNF (20 ng/mL, Peprotech) with the following chemicals: CHIR99021 (3 μM), forskolin (10 μM) and SP600125 (10 μM). The induced neurons were then fixed for immunofluorescence or pelleted for Western blot. Nikon Eclipse Ti2-E motorized inverted microscope and Zeiss LSM 800 confocal microscope were used to image the morphology of the neurons. The neuronal conversion rate (% of Tuj1+ soma/total number of cells stained with DAPI) was calculated by manually analyzing randomly selected 15 (20× magnification) fields for each line from three independent replicates by a blinded investigator. The neurite length was computed from the same set of images by using SNT plugin of image-analyzing tool, Fiji.[75]

Reprogramming of fibroblasts to astrocytes

Skin fibroblasts were directly converted to induced neuronal progenitor cells (iNPCs) by using a previously described method.[16] The iNPCs were maintained in fibronectin (2.5 μg/mL, Millipore) coated dishes and DMEM/F12 media containing 1% N2 supplement, 1% B27 and 20 ng/mL bFGF-2. To differentiate iNPCs to astrocytes, a small portion (20% of a confluent plate) of the cells was seeded onto fibronectin-coated dishes with DMEM/Glutamax (Gibco) media containing 10% FBS (Gibco) and 0.2% N2. Five days post differentiation induced astrocytes were characterized for astrocyte-specific markers (GFAP and CD44) by immunofluorescence.

Immunofluorescence

Fibroblasts (60,000 cells) and astrocytes (40,000 cells) were seeded on 24 well plates with fibronectin-coated coverslips. The next day, cells were fixed with 4% paraformaldehyde for 15 min and washed 3× with DPBS before the blocking solution consisting of DPBS with 10% goat serum (Gibco), 0.1% Triton X-100 (Sigma-Aldrich), and 0.1% Tween 20 (Fisher Scientific) was applied for 1 h. Chemically-induced neuronal cells were fixed with ice-cold 4% paraformaldehyde (Sigma-Aldrich) and 0.1% glutaraldehyde (Sigma-Aldrich) for 20 min instead, and blocked with ice-cold DPBS with 4% goat serum and 0.2% Triton for 1 h. All primary antibodies were diluted in blocking solution and their dilution and provider are listed in the key resources table. Incubation of the primary antibody was performed overnight at 4°C. The following day, cells were washed 3× in DPBS before the secondary antibody (Alexa Fluor) and DAPI (Thermo Fisher Scientific) diluted in blocking solution was applied for 1 h at room temperature. Following three washes with DPBS, the coverslips were mounted in Vectashield (Vector Labs) and sealed. Images were captured either with Nikon Eclipse Ti2-E motorized inverted microscope or the Zeiss LSM 800 confocal microscope and processed with Adobe Photoshop. Anti-IRF2BPL antibody from Novus Biologics (NBP2-14712) which has a different target site was also used to check for mislocalization in patient iAs.

Western blot

Cell pellets were lysed with RIPA lysis buffer (Thermo Fisher) followed by sonication for 10 s. Protein was quantified by DC Protein Assay (Biorad) and 50 μg of cell lysate was loaded onto 4-12% BIS-Tris PAGE gel (Thermo Fisher Scientific) and run at 120 volts for 1 h. Protein was transferred onto a PDVF membrane (Bio-rad) and blocked for 1 h at room temperature using Odyssey blocking buffer (Li-COR). Primary antibodies (key resources table) were incubated overnight at 4°C. The next day, the membrane was washed three times with Tris-Buffered Saline and 1% Tween and incubated with 1/12,000 diluted Li-COR secondaries for one hour at room temperature and washed again three times before imaging the blot using Odyssey DLx LICOR Imaging System and processed using Image Studio Lite.

Separation of nuclear and cytoplasmic protein fractions was conducted using Thermo Scientific NE-PER Nuclear and Cytoplasmic Extraction kit. Manufacturer's guidelines were followed for the fractionation. Upon quantification, 50 μg of cytoplasmic fraction and 30 μg of nuclear fraction was loaded onto the gel and run as described above. Histone 3 (H3) and β-tubulin was used as markers for nuclear and cytoplasmic fractions respectively. The extracts had less than 10% contamination between the two fractions.

mRNA SNP-genotyping

RNA was extracted from healthy and patient iAs using Trizol (Thermo Fisher Scientific) and Chloroform (Sigma-Aldrich),[76] and reverse transcribed to cDNA using RevertAid RT Reverse Transcription Kit (Thermo Fisher Scientific). To validate the expression of mutated mRNA in patients we conducted Custom TaqMan SNP genotyping assay (Thermo Fisher Scientific) involving quantitative PCR to detect wildtype IRF2BPL mRNA and patient-specific mutated mRNA (P1- c.514G>T and c.584G>T, P2- c.519C>G, P3- c.562C>T and P4- c.2122delG). Briefly, 20 ng of cDNA was mixed with 2X GTX Express master mix (Thermo Fisher Scientific) and 20X TaqMan SNP Assay mix and run on Applied Biosystems QuantStudio 6 machine. Thermo Connect platform was used to develop the SNP genotyping graphs.

HA pull-down assay and lentivirus transduction

Ha-tagged constructs. N-terminal HA-tagged IRF2BPL (human, NM_024496.3) expressing plasmid (pcDNA3.1+CMV-N-HA-*IRF2BPL*) was synthesized from GenScript. To express HA-tagged patient-specific truncated IRF2BPL, the mutated sequence from patient P1, P2 and P3 was amplified from pcDNA3.1+CMV-N-HA-*IRF2BPL* using Q5 DNA Polymerase (NEB) by designing the reverse primer with the mutated nucleotide (Table S5). The amplicons were then cloned into pcDNA3.1 plasmid and confirmed by sanger sequencing (Eurofin genomics). HA-tagged mutated sequence from patient P4 was constructed from Genscript by single point mutagenesis of pcDNA3.1+CMV-N-HA-*IRF2BPL*.

HA immunoprecipitation. The above five constructs were independently transfected into HEK293 by calcium phosphate method.[77] Briefly, HEK293 cells (1 x 10^6) were seeded onto a 6-well plate in in DMEM media containing 10% FBS and 1% Antibiotic-Antimycotic (Anti-anti) (Thermo Fisher Scientific). The next day, 2 μg of the plasmid was mixed with 250 mM calcium phosphate (Sigma-Aldrich) and equal volume of Alfa Aesar HEPES-buffered saline, pH 7.0 and was added to 80% confluent HEK293 cells. The following day the media was changed to DMEM containing 2% FBS. The cells were pelleted down after 72 h and lysed with RIPA lysis buffer for HA-immunoprecipitation using Pierce HA-Tag IP/Co-IP Kit (Thermo Fisher Scientific). Manufacturer's guidelines were followed to elute proteins interacting with the Anti-HA agarose resin. The elute was then loaded for Western blot as described above. For confocal imaging, HEK293 cells (300,000) were seeded onto a 24-well plate with coverslips and transfected with the constructs for 72 h before fixation for immunofluorescence.

Lentiviral transduction. IRF2BPL (human, NM_024496.3) expressing plasmid (*pcDNA3.1+CMV-IRF2BPL*) was synthesized by GenScript. The cDNA was then cloned into *pBOB-CMV-GFP* (addgene 12,337) by replacing the GFP sequence. Patient mutated sequence from P1, P2 and P3 was amplified as described above and cloned into the lentiviral backbone. Mutated sequence from patient P4 was constructed from GenScript by single point mutagenesis of *pcDNA3.1+CMV-IRF2BPL* and cloned into lenti-viral backbone. Viral particles were produced and concentrated by ultracentrifugation as described before.[78] The viral titer was calculated after running Lentivirus Titer qPCR (abm) and an MOI of 10 was used to infect iAs for 48 h before fixation for immunofluorescence.

Coculture assay

Coculture assay was conducted as previously described.[16] Briefly, healthy and patient iAs were treated with 1 μM CuATSM (gifted by Joseph Beckman) in dimethyl sulfoxide (DMSO) (Sigma-Aldrich) diluent, or in straight DMSO as a negative control beginning on day 2 of their differentiation for 4 days. Post 5 days differentiation, the iAs were plated in 96-well plates coated with fibronectin at a density of 10,000 per well. Mouse embryonic stem cells expressing GFP was differentiated into neurons as described previously.[16] The next day, GFP-positive neurons were sorted using Becton-Dickenson Influx sorter and suspended in neuron media consisting of DMEM/F12, 5% ES FBS (Gibco), 2% N2, 2% B27 along with growth factors GDNF (10 ng/mL), BDNF (10 ng/mL) and CNTF (Peprotech; 20 ng/mL). They were then added to iAs at a density of 10,000 per well. The coculture plate was scanned every day with the automated IN Cell Analyzer 6000 to capture GFP-positive neurons up to 3 days. The IN Cell 6000 developer and analyzer software were used to stich 16 images per 96-well and count neuronal survival. The assay was repeated 5 times and was normalized to healthy controls.

To test if knockdown of IRF2BPL in healthy iAs causes toxicity to neurons in coculture, a shRNA (sh29) targeting IRF2BPL sequence 5′-GGAGACAATCTTGCTACCTGT-3′ was designed and cloned into LV-H2B-RFP (addgene 26,001). Healthy iAs was

then infected with the lenti-virus (LV-sh29) for four days to test knockdown efficiency. For coculture assay, 4 day differentiated H1 iAs (8000 cells) were seeded into 96 well plates along with or without lenti-virus (LV-RFP, LV-FL, LV-sh29, LV-P1, LV-P2, LV-P3 and LV-P4) at an MOI of 10. Two days later, the cells transduced with virus expressing truncated IRF2BPL proteins were treated with 1 μM CuATSM and the other conditions with same volume of DMSO. After 5 h, GFP positive neurons were seeded on top of the iAs and its viability was assessed for each condition as described above.

For the condition media experiment, control and patient iAs were seeded at a density of 10,000 per well in fibronectin-coated 96 well plate (day 0) and on the following day (day 1) the astrocyte media was replaced with neuron media (components described above). Simultaneously on day 1, GFP + mouse neurons were seeded at the same density in poly-lysine and laminin coated 96 well plate with fresh neuron media. Twenty-four hours later (day 2), media of the neurons was replaced with 60% condition media from each iAs cell line. On day 3, the media was replaced again. 48 h post culturing with condition media, the neuronal survival was assessed for each condition on day 4. Neg Ctl neuron wells were included in the assay which involved replacing media with fresh neuron media instead of condition media.

Computational analysis of mitochondria

The culture supernatant from human iAs was tested for any contamination with mycoplasma using Agilent's Mycosensor PCR Assay kit, before fixing cells for mitochondrial analysis. The cells were immuno-stained with anti-COXIV (key resources table) to visualize and examine mitochondrial networks. Image analysis was performed using CellProfiler 4.2.0. Nuclei were segmented using three level Otsu and object separated with watershed. Mitochondria were segmented by first applying non-local mean denoising, enhancing the mitochondrial structures with the tubeness algorithm and segmented with three level Otsu. Intensity and morphological parameters were measured for segmented objects and the resulting data was analyzed with KNIME 4.3.1. The area of mitochondria was summed and divided by the number of nuclei for each cell line and replicated to obtain the total area of mitochondria per cell. The number of mitochondria was counted, summed, and divided by the total area of mitochondria for each cell line and replicated to obtain the number of mitochondria normalized to the total area. We called this second parameter ''fractionation index'' as it was proportional to how fractionated the mitochondrial network was.

Seahorse ATP real-time rate assay

Differentiated astrocytes (iAs) were seeded into 96-well seahorse plates in 5–6 replicates. Manufacturer's (Agilent) guidelines were followed to set up the plates for ATP rate assay. The base oxygen consumption rate (basalOCR) was measured at three different time points using automated Seahorse XFe96 Analyzer (Agilent). Next, oligomycin (1.5 μM), an inhibitor of the ATP synthase was injected, and three additional measurements were read (oligoOCR). The ATP-linked respiration was calculated by subtracting the basalOCR from the oligoOCR. Lastly, antimycin A and rotenone (0.5 μM) was injected into the wells to measure the non-mitochondrial respiration which was subtracted from all readings. The live cells were stained with Hoechst 33,342 (1: 2000) for 15 min and then counted by ImageJ macro created in our laboratory. All the readings were normalized to the number of cells per well.

RNA-seq analysis

Five-day differentiated iAs were pelleted down for RNA-seq processing. Raw sequencing reads were mapped to the human genome (GRCh38 assembly) using STAR version 2.7.1a[79] using default settings, except –outFilterMismatchNoverLmax, which was set to 0.05. Reads were counted using htseq-count 0.9.1[80] with GENCODE release 27 gene annotation.[81] Differential gene expression analysis was performed using the DESeq2 (version 1.30.1) R package.[82] Gene expression values were *Z* score transformed, clustered and plotted as heatmaps using the pheatmap[83] package in R. High throughput RNA-seq datasets are deposited into NCBI Gene Expression Omnibus (GEO) repository according to MIAME-compliant data submissions, NCBI GEO: GSE189909).

RNA-seq data was confirmed by qPCR of a set of genes run on Applied Biosystems 7500. Primers used for the reactions are listed in Table S6.

Colocalization in Drosophila. Briefly, immunostaining was performed as previous described.[84] The wing discs from third instar larva were dissected in ice-cold PBS. Discs were then fixed in 4% PFA followed by three washes in 0.2% PBST. The discs were incubated in primary antibodies in blocking solution (0.8% normal goat serum) overnight at 4°C. The next day, discs were washed in 0.2% PBST and incubated with corresponding secondary antibodies (Jackson ImmunoResearch) and DAPI for 90 min at room temperature. Finally, the discs were washed three times in PBST and mounted in Vectashield (Vector Labs). Imaging was carried out in Zeiss 880 microscope and processed with Adobe photoshop.

Drosophila climbing assay. Climbing (negative geotaxis) assays were performed as previously described.[72] Briefly, flies were anesthetized 24 h prior to testing using CO_2 and housed individually. On the testing day, flies were transferred to a clean, empty vial and given 1 min to habituate before being tapped to the bottom of the vial and assessed for a negative geotaxis response. Flies were given a maximum of 30 s to reach 7 cm. All flies were females of indicated genotypes and reared at 25°C. Flies were transferred into a fresh vial every 3 days. At least 20 flies were tested per genotype.

CuATSM treatment in flies. Parental crosses of either $Pits^{MiMIC}$ or $Pits^{TG4}$ females were crossed to control (*CantonS*) males on 10 mL of standard molasses-based fly food containing either 25μL of either DMSO or CuATSM (50 μM – final concentration) dissolved in the molten food. Upon eclosure from pupae, adult heterozygous flies of the appropriate genotype ($Pits^{MiMIC}$/+ or $Pits^{TG4}$/+) were transferred to fresh vials containing 5 mL of fly food containing 12.5μL of either DMSO or CuATSM (50 μM – final concentration). Flies

were transferred into fresh vials with drugs treaments every two days until reaching the appropriate age for behavioral assessment.

ATP assessment in flies. ATP levels were measured as described previously.[85] 10-15 heads from each genotype were taken for one set of experiment. Total levels of ATP was measured using ATP determination kit (A22066, Life Technologies) as per manufacturer's instruction.

QUANTIFICATION AND STATISTICAL ANALYSIS

Results are presented as dot or boxplots, in which the mean ± standard error of the mean (SEM) are depicted. All statistical analysis was performed using Graphpad Prism (GraphPad Software, Inc., Ca, US). When the means of 2 groups were compared, a two-tailed unpaired t test was used. When more than 2 groups were analyzed, ANOVA was employed with Dunnett's multiple comparison test between the mean of the controls and the mean of each line was computed to derive the p value (p). ANOVA followed by Tukey's LSD was used for computing the significance for *in vivo* experiments. Results were designated significant when the p value (p) < 0.05: * = $p < 0.05$, ** = $p < 0.01$,*** = $p < 0.001$, **** = $p < 0.0001$, ns = non-significant.

Cell Reports, Volume *41*

Supplemental information

Mechanisms of IRF2BPL-related disorders and identification of a potential therapeutic strategy

Shrestha Sinha Ray, Debdeep Dutta, Cassandra Dennys, Samantha Powers, Florence Roussel, Pawel Lisowski, Petar Glažar, Xiaojin Zhang, Pipasha Biswas, Joseph R. Caporale, Nikolaus Rajewsky, Marc Bickle, Nicolas Wein, Hugo J. Bellen, Shibi Likhite, Paul C. Marcogliese, and Kathrin C. Meyer

Table S1: Cell lines used in the study.

Cell line	Age (yrs)	Mutation	Gender	Status	Disease severity
H1	8	N/A	Male	Healthy child	N/A
H2	8	N/A	Female	Healthy child	N/A
H3	65	N/A	Female	Healthy adult	N/A
H4	36	N/A	Male	Healthy adult	N/A
P1	12	p.E172X and p.G195V	Male	Child patient	Severe developmental regression[S1]
P2	10	p.Y173X	Male	Child patient	Severe developmental regression[S2]
P3	21	p.R188X	Male	Adult patient	Severe developmental regression[S1,2]
P4	3	p.A708Fs59	Male	Child patient	Mild developmental delay[S2]

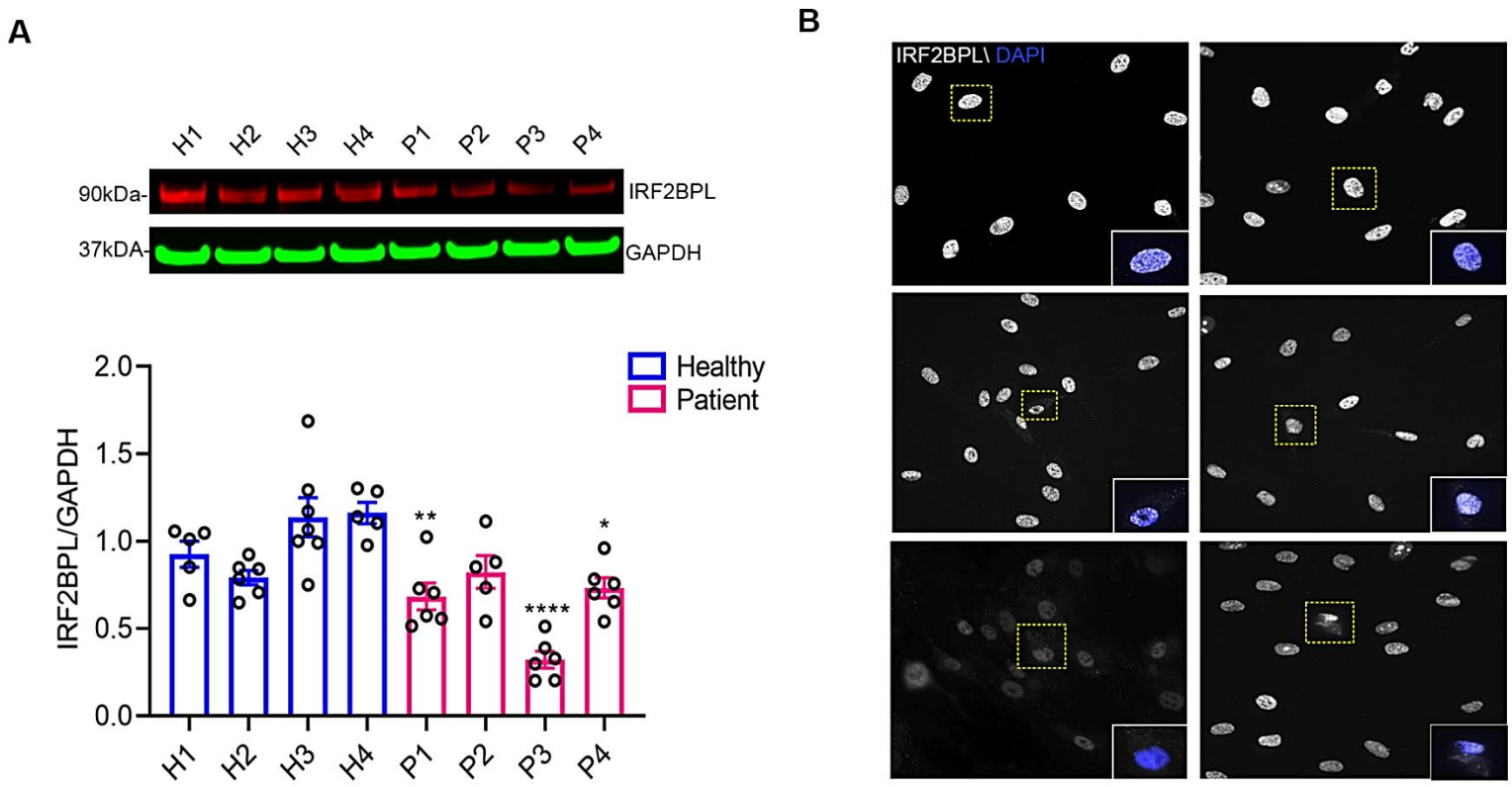

Figure S1: Comparison of IRF2BPL protein expression between NEDAMSS and healthy fibroblasts (A) and (B) show IRF2BPL expression levels of healthy and NEDAMSS fibroblasts by western blot and immunocytochemistry respectively. Only adult patient P3, shows approximately 50% lower expression compared to healthy lines. IRF2BPL protein smears are faintly seen in the cytoplasm of patient fibroblasts. Yellow dotted rectangles represent the merged image of DAPI and IRF2BPL stained cells seen in the corner white boxes (dimensions of image 40 µm x 50 µm) of each fibroblast cell line. ANOVA followed by Dunnett's multiple comparison test between the mean of the controls and the mean of each line was computed to derive the P value (p), * = $p < 0.05$, ** = $p < 0.01$, *** = $p < 0.001$, **** = $p < 0.0001$. Scale bar = 50µm.

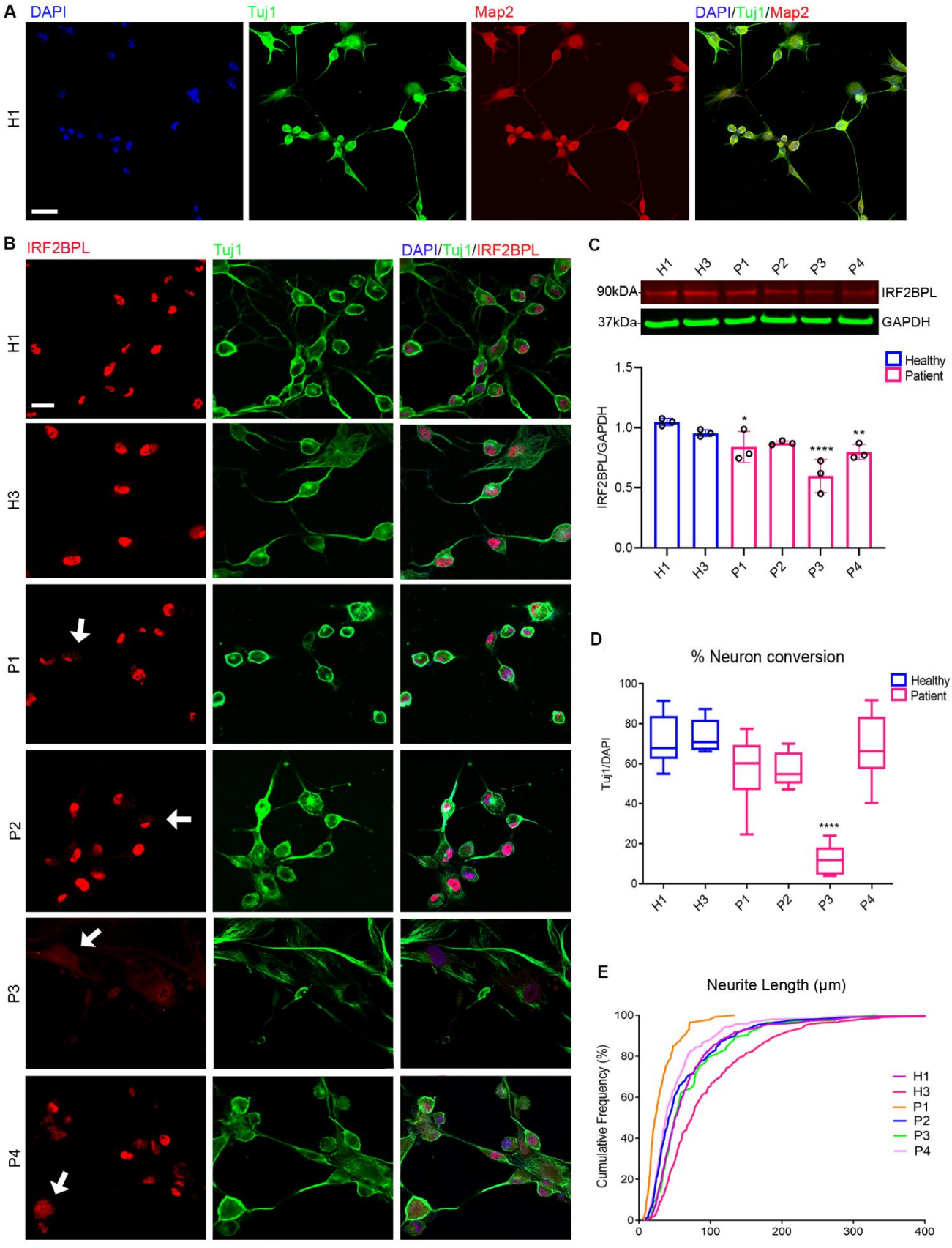
A
DAPI
Tuj1
Map2
DAPI/Tuj1/Map2
H1
B
IRF2BPL
Tuj1
DAPI/Tuj1/IRF2BPL
H1
H3
P1
P2
P3
P4
C
H1
H3
P1
P2
P3
P4
90kDA-
IRF2BPL
37kDa-
GAPDH
Healthy
Patient
IRF2BPL/GAPDH
1.5
1.0
0.5
0.0
*
****
**
D
% Neuron conversion
Healthy
Patient
Tuj1/DAPI
100
80
60
40
20
0
****
E
Neurite Length (μm)
Cumulative Frequency (%)
100
80
60
40
20
0
0
100
200
300
400
H1
H3
P1
P2
P3
P4

Figure S2: NEDAMSS patient neurons exhibit variable phenotype. Fibroblasts were directly converted to neurons (iNs) using seven small molecules: VPA, CHIR99021, repsox, forskolin, SP600125, GO6983 and Y-27632 (A) Flourescent microscope imaging at 40X magnification shows directly converted iNs from H1 fibroblasts express neuron specific markers Tuj1 and MAP2 on day 7. (B) Confocal two-dimensional imaging (63X/1.4 Oil magnification) shows IRF2BPL protein present as faint smears in the cytoplasm of Tuj1+ day 7 patient iNs in comparison to healthy iNs. White arrows indicate the protein smears. A representative image was selected for each line from three independent culture replicates (C) Western blot of IRF2BPL expression levels in healthy and patient iNs reveals the most significant loss of protein in line P3. Protein lysates from three replicates were tested (D) Neuronal conversion rate (% Tuj1 positive cells over total DAPI stained cells) and their (E) neurite length on day 7 indicates a range of phenotypes among NEDAMSS patient iNs, with patient P3 exhibiting significantly lower conversion rate and patients P1 and P3 displaying shorter neurite length. A total of 15 fields captured at 20X magnification from three differentiation experiments was analyzed by using ImageJ software. ANOVA followed by Dunnett's multiple comparison test between the mean of the controls and the mean of each line was computed to derive the P value (p), * = $p < 0.05$, ** = $p < 0.01$, *** = $p < 0.001$, **** = $p < 0.0001$. Scale bar for (a) 50µm and for (b) 20µm.

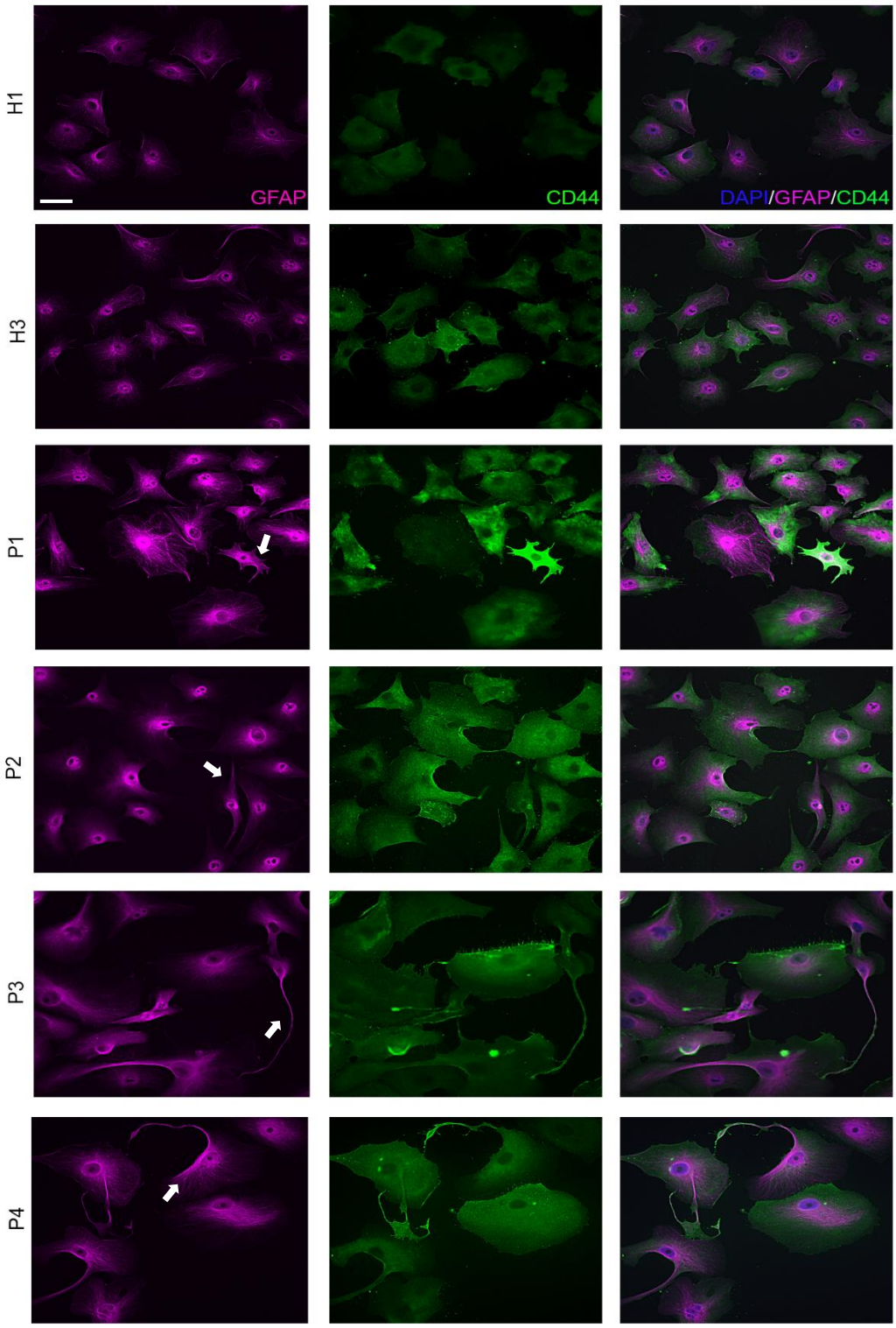

Figure S3: Characterization of differentiated astrocytes (iAs) from healthy and patient iNPCs. Healthy and NEDAMSS patient iAs are positive for astrocyte-specific markers GFAP and CD44. Patient iAs exhibit an activated phenotype compared to healthy iAs. Images from three independent experiments were captured at 40X magnification with Nikon Eclipse Ti2-E microscope. White arrows indicate morphological differences in NEDAMSS patient iAs compared to healthy cell lines. Scale bar = 50µm.

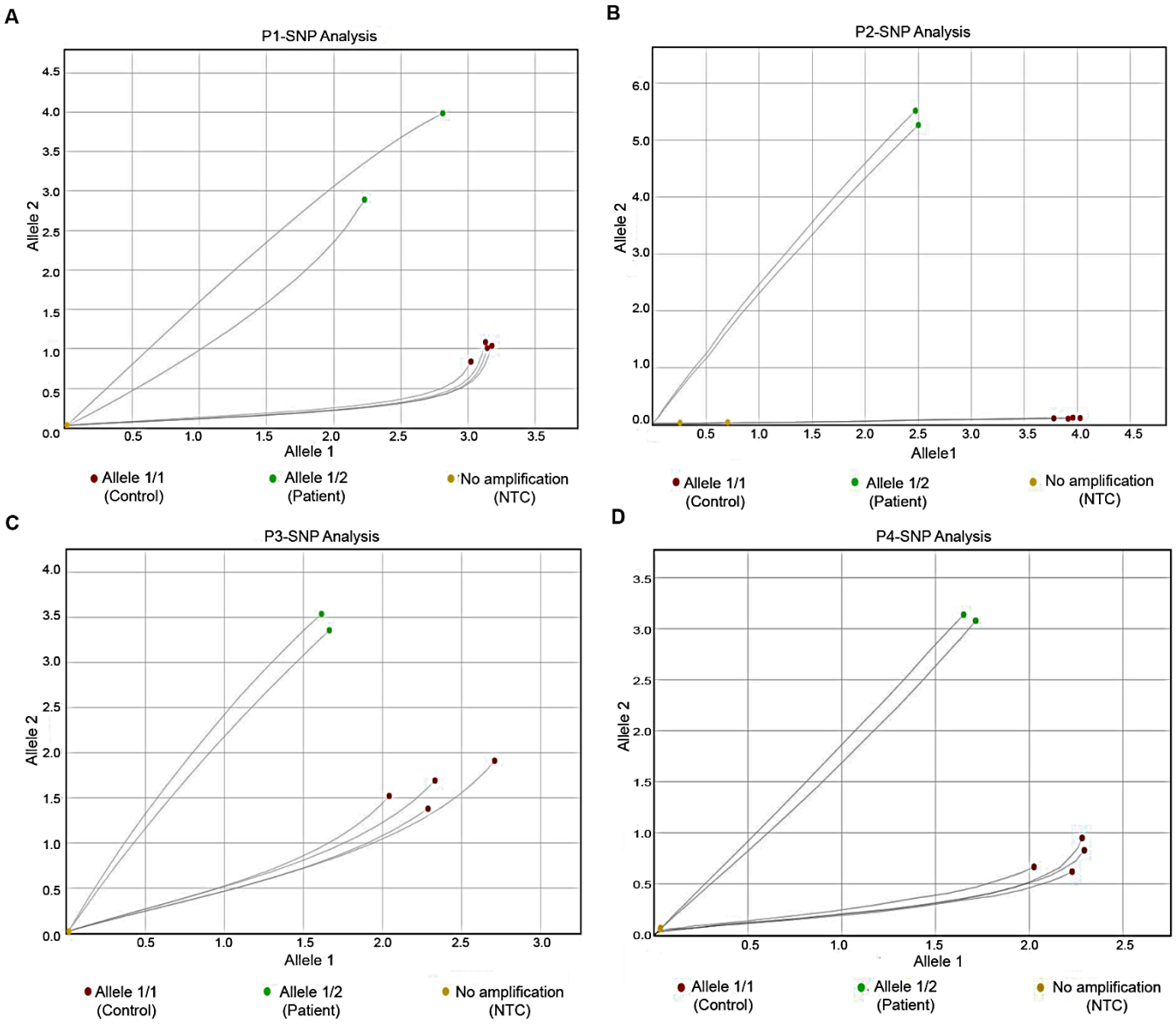

Figure S4: SNP genotyping analysis to detect the presence of mutant mRNA in patients. RNA from differentiated iAs from healthy lines (H1 and H3) and NEDAMSS patients (P1, P2, P3 and P4) was extracted and transcribed to cDNA. Customized SNP genotyping assay was conducted to detect the presence of the mutated and wildtype IRF2BPL mRNA in (A) P1 (c.514G>T and c.584G>T) (B) P2 (c.519C>G) (C) P3 (c.562C>T) and (D) P4 (c.2122delG) compared to healthy controls. Two different cell passages from each patient and control were used for the SNP analysis. The assay was repeated three times.

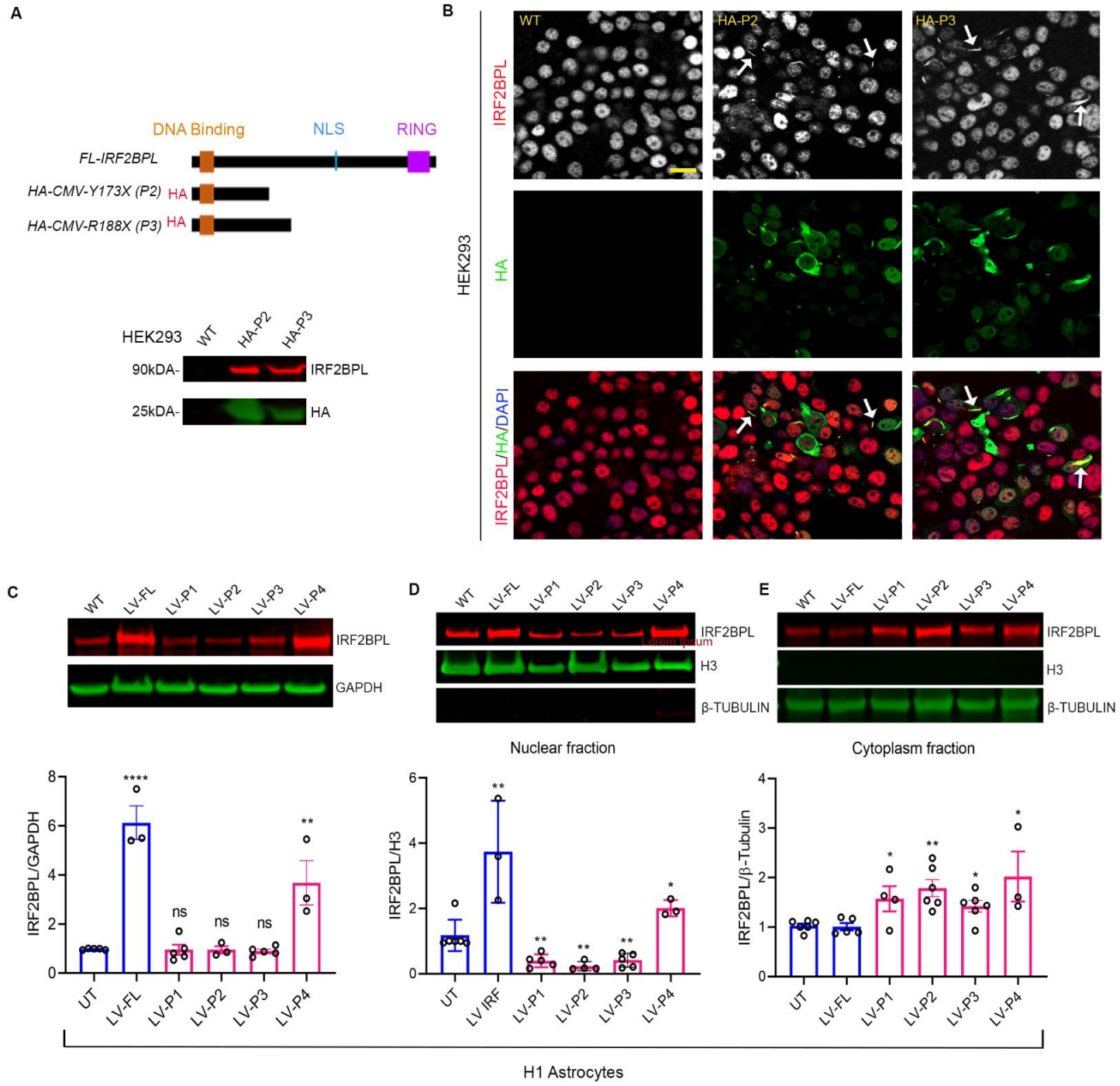

Figure S5: Overexpression of mutant IRF2BPL protein dimerizes with full length (FL) IRF2BPL and causes sequestration of the protein to the cytoplasm in HEK293s and in wildtype astrocyte line H1. (A) Schematic of constructs expressing N-terminal HA-tagged truncated IRF2BPL proteins (*HA-CMV-P2* and *HA-CMV-P3*). These constructs were transfected into HEK293s and pelleted down for HA pull down assay after 72 hours. HA elute blot confirms that FL-IRF2BPL (white, anti-IRF2BPL) and HA-tagged truncated IRF2BPL P2 or P3 (green, anti-HA) can bind to each other, as seen in lanes 2 and 3. (B) Confocal imaging indicates mis-localization of FL-IRF2BPL to the cytoplasm of HEK293 cells transfected with the constructs. White arrows point to FL-IRF2BPL protein mislocalized to the cytoplasm. Two-dimensional images were captured at 63X/1.4 Oil magnification covering 9 random fields from three independent replicates. (C) Healthy H1 iAs was transduced with lenti-virus (LV) expressing FL-IRF2BPL or the patient-derived truncated proteins for 4 days and pelleted down for western blot. LV-FL and LV-P4 showed higher levels of total IRF2BPL protein

expression compared to un-transduced (UT) astrocytes. Fractionation studies conducted on the same pellets revealed lower levels of IRF2BPL in the (D) nuclear fraction (normalized to nuclear marker H3) for iAs transduced with LV-P1, LV-P2 and LV-P3 and higher levels in the (E) cytoplasm fraction (normalized to cytoplasmic marker β-Tubulin), which further confirms sequestration of the full length to the cytoplasm by mutant proteins. All experiments were conducted with a minimum of three independent culture repeats. Unpaired t-test was conducted between un-transduced (UT) and each LV condition to derive the P value (p), * = $p < 0.05$, ** = $p < 0.01$, *** = $p < 0.001$, **** = $p < 0.0001$, ns = not significant. Scale bar = 50µm.

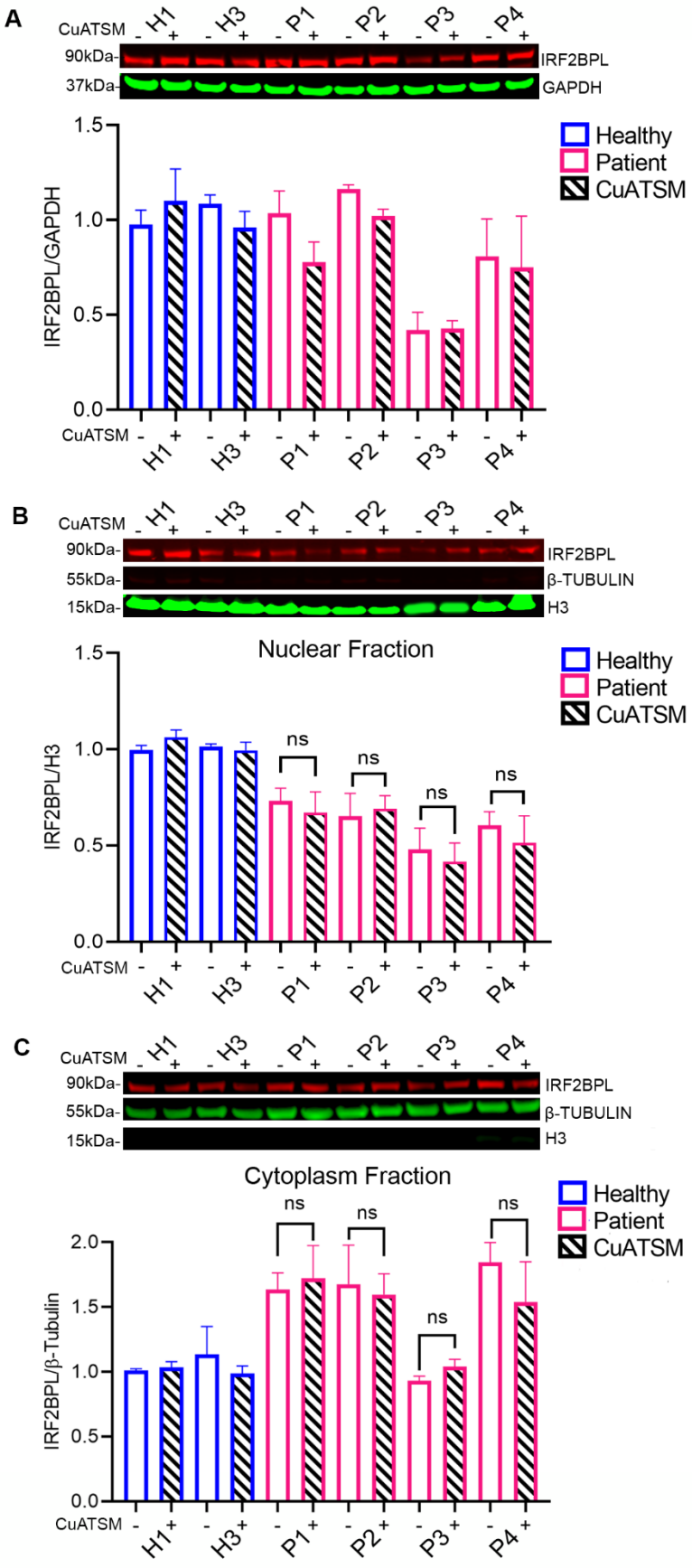
A
CuATSM - + - + - + - + - + - +
H1 H3 P1 P2 P3 P4
90kDa-
37kDa-
IRF2BPL
GAPDH
IRF2BPL/GAPDH
1.5
1.0
0.5
0.0
Healthy
Patient
CuATSM
B
90kDa-
55kDa-
15kDa-
IRF2BPL
β-TUBULIN
H3
Nuclear Fraction
IRF2BPL/H3
ns
C
Cytoplasm Fraction
IRF2BPL/β-Tubulin
2.0

Figure S6: CuATSM does not impact IRF2BPL expression levels or sequestration of the protein in patients. (A) Treatment with CuATSM does not change the overall expression of IRF2BPL in heathy and patient iAs. (B) Nuclear and (C) cytoplasmic fractions do not show any difference with drug treatment. Three independent culture replicates were used for the western blot. Unpaired t-test was conducted between untreated and treated groups to compute p value. ns= not significant.

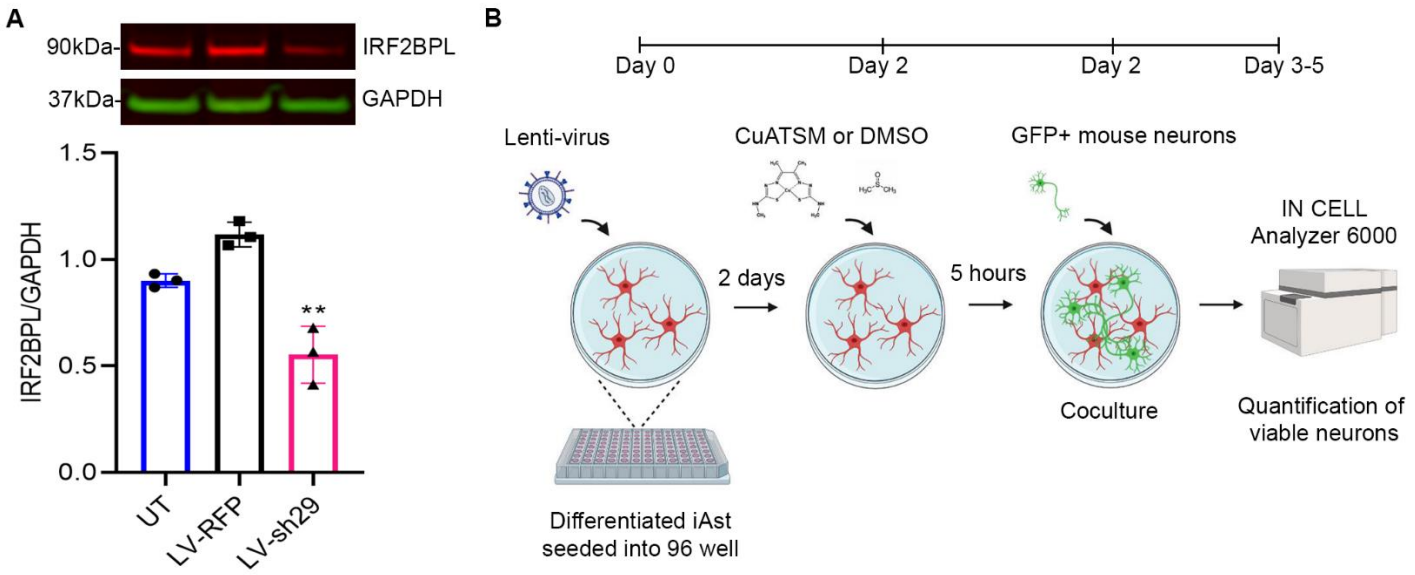

Figure S7: Knockdown of IRF2BPL protein by lentivirus expressing shRNA in H1 iAs. (A) H1 iAs was transduced with LV-RFP and LV-sh29 (expressing RFP and shRNA against IRF2BPL respectively) at an MOI of 10 and pelleted down after 4 days to assess the knockdown of protein by western blot. Experiment was repeated three times. Unpaired t-test was conducted between un-transduced (UT) iAs and LV-sh29 transduced iAs to compute P value (p). ** $p<0.01$. (B) Schematic of coculture assay depicts seeding of lentivirus (LV) transduced iAs with GFP+ mouse neurons. On day 2, CuATSM (1 µM) or DMSO was added to iAs, 5 hours before coculture with neurons. Illustration was created by using biorender.com.

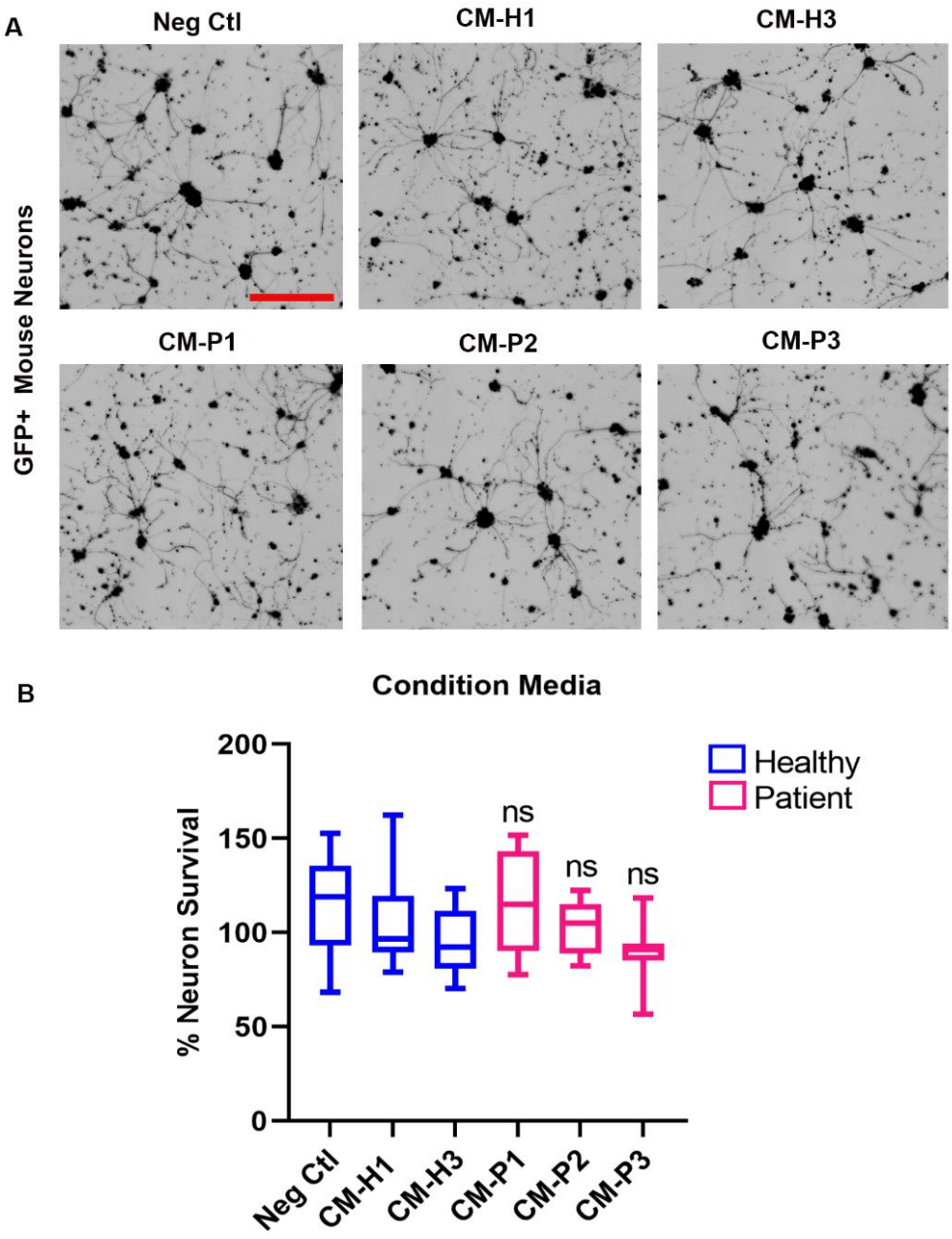

Figure S8: Condition media of NEDAMSS iAs has no effect on neuron viability. Control and patient iAs were seeded in triplicates in a 96 well plate (day 0) and the following day (day 1) the astrocyte media was replaced with neuron media. On day 1, GFP+ mouse neurons were seeded in triplicates in poly-lysine and laminin coated 96 well plate with fresh neuron media. For the next two days (day 2 and day 3), media of the neurons was replaced with 60% condition neuron media (CM) from each iAs cell line. Neg Ctl wells were replaced with fresh neuron media instead of CM. (A) Representative images of GFP+ mouse neurons (shown in black) following 48 hours in CM (day 4). (B) Quantification of neuronal survival on day 4 shows no significant loss of neuronal survival with patient iAs condition media compared to controls. Data was normalized to average neuronal survival of healthy controls and represents 3 independent culture repeats. ANOVA followed by Dunnett's multiple comparison test between the mean of the controls and the mean of each line was computed to derive the P value (p), ns= not significant. Scale bar= 200µm.

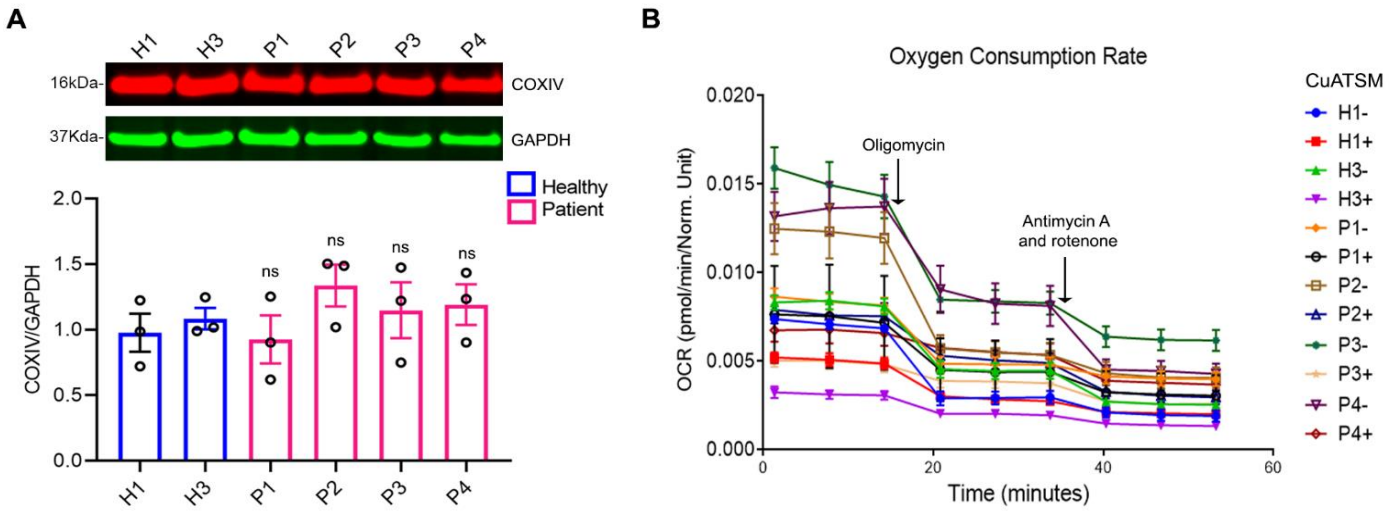

Figure S9: Mitochondrial COXIV expression remains intact in NEDAMSS iAs but the oxygen consumption rate shows elevated levels. (A) Differentiated iAs from healthy controls and patients were pelleted down after 5 days to quantify the expression levels of COXIV, a mitochondrial marker. ANOVA followed by Dunnett's multiple comparison test between the mean of the controls and the mean of each line was computed to derive the P value (p), ns= not significant, (B) Oxygen consumption rate (OCR) of iAs computed from Seahorse ATP rate assay with and without treatment with CuATSM. Experiment was repeated with three independent culture replicates.

Table S3: Thirty-seven common differentially expressed genes in patient iAs. [Reference]

	Log 2 FC	P Adjusted	Neuronal Function, Growth, Development, Support, Neurological Diseases	Mitochondria, Metabolism, Oxidation, Apoptosis
REG3G	-8.3000	0.03787		[S3,4]
LINC01593	-5.2000	0.01323		
SSTR2	-4.2600	0.01394	[S5-7]	[S7-9]
ABCA8	-3.8000	0.00893	[S10,11]	
ANKS1B	-3.6400	0.00563	[S12-18]	
LINC00639	-3.5900	0.00978		
CADPS	-3.1400	0.00008	[S19-22]	
EGR2	-3.1400	0.01323	[S23-28]	[S28,29]
UGT1A7	-3.0300	0.00281	[S30]	
LMOD1	-2.7100	0.00363		
AC138305.1	-2.2100	0.00746		
FAM71F1	-2.0700	0.02580		
KLF2	-1.6100	0.02705	[S31-33]	[S34-36]
STK32C	-1.2900	0.02462	[S37-39]	
SEMA4G	-1.0400	0.00056	[S40-43]	
MOCS1	-1.0100	0.01414	[S44-47]	[S48,49]
GRIP2	-0.6800	0.04881	[S50-52]	
NUDT18	-0.6300	0.04849		
ADGRF5	6.4800	0.00746		
GREB1L	5.2900	0.02536	[S53,54]	
ADGRV1	4.7600	0.00019	[S55-58]	
CDSN	4.6800	0.03052		
NLRP2	4.6100	0.02821	[S59,60]	
NRG2	4.4300	0.03979	[S61-64]	
GLDC	4.2600	0.00746	[S65,66]	
CPPED1	3.0400	0.00069		
PHACTR1	2.8500	0.02536	[S67-69]	
C6orf141	2.7700	0.00007		
ZNF469	2.3700	0.03713		
TNFAIP8	2.2900	0.02705		[S70-72]
DMKN	1.7300	0.03052		
EPB41L4B	1.5200	0.03713		
AKT3	1.4700	0.03713	[S73-76]	[S77,78]
]PLCXD2	1.4600	0.03052		
BTBD3	1.1100	0.04881	[S79,80]	
UBASH3B	1.0300	0.04013		
CYP4V2	0.9300	0.04881		

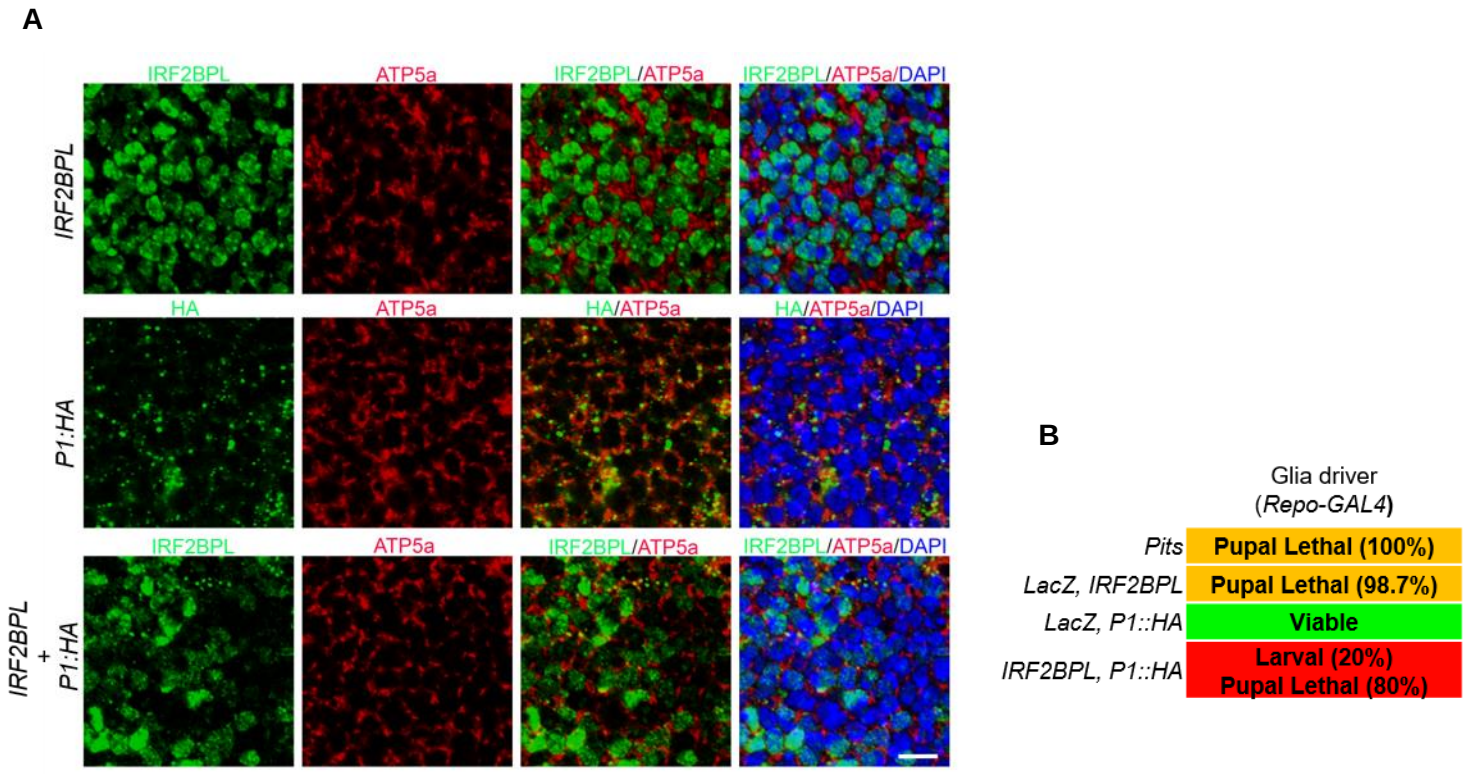

Figure S10: Overexpression of human IRF2BPL and patient-related truncation in *Drosophila* causes mislocalization of full-length IRF2BPL and causes pupal lethality. (A) Overexpression of *UAS-IRF2BPL* alone by nubbin-GAL4 driver, is primarily localized to nucleus in the wing pouch of *Drosophila* (anti-IRF2BPL in green), whereas *UAS-IRF2BPLp.E172X::HA* (*P1::HA*) alone is found mislocalized to the cytoplasm (anti-HA in green). When both the constructs are co-expressed, the full-length IRF2BPL is seen mislocalized to the cytoplasm (anti-IRF2BPL in green). ATP5a in red is a mitochondrial marker used. Scale bar = 2µm. (B) Overexpression of UAS-IRF2BPL in glia using Repo-GAL4 at 29°C causes pupal lethality. Overexpression of *UAS-IRF2BPLp.E172X::HA* alone leads to viable adults, however co-expression of full-length *UAS-IRF2BPL* and truncated *UAS-IRF2BPLp.E172X::HA* lead to larval and pupal lethality. These data indicate that there may be a toxic effect when both full-length and truncated proteins are expressed.

Table S5: List of primers used for mutagenesis

Construct	Forward primer (5'-3')	Reverse primer (5'-3')
pCDNA-HA-P1	GCCACCATGTACCCATACG	CTAGAAGCGGCTGCGCTGTTCCA
pCDNA-HA-P2	GCCACCATGTACCCATACG	CTACTCGAAGCGGCTGCGCTGTT
pCDNA-HA-P3	GCCACCATGTACCCATACG	TCACGCGGTGTGGCTGCTGCTT
UAS-P1::HA	GACCCAGCTTTCTTGTACAAAGTTG	GAAGCGGCTGCGCTGTTC

Table S6: List of primers used for quantitative PCR in the study

Gene	Forward primer (5'-3')	Reverse primer (5'-3')
SSTR2	CTGTGTACCAAGCCCCAGAT	GATGATCACCATGGCTGTGT
ERG2	GTGACCATCTTTCCCAATGC	TTGCCCATGTAAGTGAAGGTC
AKT3	CGGAAAGATTGTGTACCGTGATC	CTTCATGGTGGCTGCATCTGTG
NGR2	CAGAAGAGGGTCCTGACCATCA	GAGGTGGTTGTGCATCTGCTTC

References

S1. Marcogliese, P.C., Shashi, V., Spillmann, R.C., Stong, N., Rosenfeld, J.A., Koenig, M.K., Martinez-Agosto, J.A., Herzog, M., Chen, A.H., Dickson, P.I., et al. (2018). IRF2BPL Is Associated with Neurological Phenotypes. Am J Hum Genet *103*, 245-260. 10.1016/j.ajhg.2018.07.006.

S2. Tran Mau-Them, F., Guibaud, L., Duplomb, L., Keren, B., Lindstrom, K., Marey, I., Mochel, F., van den Boogaard, M.J., Oegema, R., Nava, C., et al. (2019). De novo truncating variants in the intronless IRF2BPL are responsible for developmental epileptic encephalopathy. Genet Med *21*, 1008-1014. 10.1038/s41436-018-0143-0.

S3. Chen, Z., Downing, S., and Tzanakakis, E.S. (2019). Four Decades After the Discovery of Regenerating Islet-Derived (Reg) Proteins: Current Understanding and Challenges. Front Cell Dev Biol *7*. 10.3389/FCELL.2019.00235.

S4. Xiang, M., Li, S., Zhou, H., Xie, M., Zhang, Z., Gou, J., Yang, J., Tian, C., Ma, K., Lu, Y., et al. (2021). Reg3g ameliorates Tacrolimus-induced pancreatic β cell dysfunction by restoring mitochondrial function. Authorea. 10.22541/AU.161695374.47072563/V1.

S5. Bowman, B.R., Bokiniec, P., McMullan, S., Goodchild, A.K., and Burke, P.G.R. (2019). Somatostatin 2 Receptors in the Spinal Cord Tonically Restrain Thermogenic, Cardiac and Other Sympathetic Outflows. Front Neurosci *0*, 121. 10.3389/FNINS.2019.00121.

S6. Kumar, U. (2005). Expression of somatostatin receptor subtypes (SSTR1–5) in Alzheimer's disease brain: An immunohistochemical analysis. Neuroscience *134*, 525-538. 10.1016/J.NEUROSCIENCE.2005.04.001.

S7. Stumm, R.K., Zhou, C., Schulz, S., Endres, M., Kronenberg, G., Allen, J.P., Tulipano, G., and Hollt, V. (2004). Somatostatin receptor 2 is activated in cortical neurons and contributes to neurodegeneration after focal ischemia. J Neurosci *24*, 11404-11415. 10.1523/JNEUROSCI.3834-04.2004.

S8. Lehman, J., Hoeksema, M., Qian, J., Chen, H., Shi, C., Eisenberg, R., and Massion, P.P. (2016). Loss of somatostatin receptor 2 expression and cellular metabolism and survival in small cell lung cancer. ASCO *34*, e20090-e20090. 10.1200/JCO.2016.34.15_SUPPL.E20090.

S9. Maduro, V., Pusey, B.N., Cherukuri, P.F., Atkins, P., Du Souich, C., Rupps, R., Limbos, M., Adams, D.R., Bhatt, S.S., Eydoux, P., et al. (2016). Complex translocation disrupting TCF4 and altering TCF4 isoform expression segregates as mild autosomal dominant intellectual disability. Orphanet J Rare Dis *11*. 10.1186/s13023-016-0439-6.

S10. Bleasel, J.M., Hsiao, J.-H.T., Halliday, G.M., and Kim, W.S. (2013). Increased Expression of ABCA8 in Multiple System Atrophy Brain is Associated with Changes in Pathogenic Proteins. J Parkinson's Dis *3*, 331-339. 10.3233/JPD-130203.

S11. Kim, Woojin S., Hsiao, J.-Hsiang T., Bhatia, S., Glaros, Elias N., Don, Anthony S., Tsuruoka, S., Shannon Weickert, C., and Halliday, Glenda M. (2013). ABCA8 stimulates sphingomyelin production in oligodendrocytes. Biochem J *452*, 401-410. 10.1042/BJ20121764.

S12. Carbonell, A.U., Cho, C.H., Tindi, J.O., Counts, P.A., Bates, J.C., Erdjument-Bromage, H., Cvejic, S., Iaboni, A., Kvint, I., Rosensaft, J., et al. (2019). Haploinsufficiency in the ANKS1B gene encoding AIDA-1 leads to a neurodevelopmental syndrome. Nat Commun*10*, 1-15.

S13. Dosemeci, A., Toy, D., Reese, T.S., and Tao-Cheng, J.-H. (2015). AIDA-1 Moves out of the Postsynaptic Density Core under Excitatory Conditions. PLOS ONE *10*, e0137216. 10.1371/JOURNAL.PONE.0137216.

S14. Ghersi, E., Vito, P., Lopez, P., Abdallah, M., and D'Adamio, L. (2004). The intracellular localization of amyloid beta protein precursor (AbetaPP) intracellular domain associated protein-1 (AIDA-1) is regulated by AbetaPP and alternative splicing. J Alzeimer's Dis *6*, 67-78. 10.3233/JAD-2004-6108.

S15. Jacob, A.L., Jordan, B.A., and Weinberg, R.J. (2010). The organization of amyloid-β protein precursor intracellular domain-associated protein-1 in the rat forebrain. J Comp Neurol *518*, 3221. 10.1002/CNE.22394.
S16. Jordan, B.A., Fernholz, B.D., Khatri, L., and Ziff, E.B. (2007). Activity-dependent AIDA-1 nuclear signaling regulates nucleolar numbers and protein synthesis in neurons. Nat Neurosci *10*, 427-435. 10.1038/nn1867.
S17. Shi, M., Huang, X.-Y., Ren, X.-Y., Wei, X.-Y., Ma, Y., Lin, Z.-Z., Liu, D.-T., Song, L., Zhao, T.-J., Li, G., et al. (2021). AIDA directly connects sympathetic innervation to adaptive thermogenesis by UCP1. Nat Cell Biol *23*, 268-277. 10.1038/s41556-021-00642-9.
S18. Tindi, J., Chávez, A., Cvejic, S., Calvo-Ochoa, E., Castillo, P., and Jordan, B. (2015). ANKS1B Gene Product AIDA-1 Controls Hippocampal Synaptic Transmission by Regulating GluN2B Subunit Localization. J Neurosci *35*, 8986-8996. 10.1523/JNEUROSCI.4029-14.2015.
S19. Ishii, C., Shibano, N., Yamazaki, M., Arima, T., Kato, Y., Ishii, Y., Shinoda, Y., Fukazawa, Y., Sadakata, T., Sano, Y., and Furuichi, T. (2021). CAPS1 is involved in hippocampal synaptic plasticity and hippocampus-associated learning. Sci Rep *11*, 1-15. 10.1038/s41598-021-88009-w.
S20. Sadakata, T., Kakegawa, W., Shinoda, Y., Hosono, M., Katoh-Semba, R., Sekine, Y., Sato, Y., Tanaka, M., Iwasato, T., Itohara, S., et al. (2013). CAPS1 Deficiency Perturbs Dense-Core Vesicle Trafficking and Golgi Structure and Reduces Presynaptic Release Probability in the Mouse Brain. J Neurosci *33*, 17326-17334. 10.1523/JNEUROSCI.2777-13.2013.
S21. Shinoda, Y., Ishii, C., Fukazawa, Y., Sadakata, T., Ishii, Y., Sano, Y., Iwasato, T., Itohara, S., and Furuichi, T. (2016). CAPS1 stabilizes the state of readily releasable synaptic vesicles to fusion competence at CA3–CA1 synapses in adult hippocampus. Sci Rep *6*, 1-8. 10.1038/srep31540.
S22. Shumate, K.M., Tas, S.T., Kavalali, E.T., Emeson, R.B., KM, S., ST, T., ET, K., RB, E., Shumate, K.M., Tas, S.T., et al. (2021). RNA editing-mediated regulation of calcium-dependent activator protein for secretion (CAPS1) localization and its impact on synaptic transmission. J Neurochem *158*, 182-196. 10.1111/JNC.15372.
S23. Blanco-Canto, M.E., Patel, N., Velasco-Aviles, S., Casillas-Bajo, A., Salas-Felipe, J., Garcia-Escriva, A., Diaz-Marin, C., and Cabedo, H. (2020). Novel EGR2 variant that associates with Charcot-Marie-Tooth disease when combined with lipopolysaccharide-induced TNF-alpha factor T49M polymorphism. Neurol Genet *6*, e407. 10.1212/NXG.0000000000000407.
S24. Boerkoel, C.F., Takashima, H., Bacino, C.A., Daentl, D., and Lupski, J.R. (2001). EGR2 mutation R359W causes a spectrum of Dejerine-Sottas neuropathy. Neurogenetics *3*, 153-157. 10.1007/S100480100107.
S25. Kim, S.H., Song, J.Y., Joo, E.J., Lee, K.Y., Shin, S.Y., Lee, Y.H., Ahn, Y.M., and Kim, Y.S. (2011). Genetic association of the EGR2 gene with bipolar disorder in Korea. Exp Mol Med *44*, 121-129. 10.3858/emm.2012.44.2.007.
S26. Mukherjee, D., Gonzales, B.J., Ashwal-Fluss, R., Turm, H., Groysman, M., and Citri, A. (2021). Egr2 induction in SPNs of the ventrolateral striatum contributes to cocaine place preference in mice. eLife *10*. 10.7554/ELIFE.65228.
S27. Nagarajan, R., Svaren, J., Le, N., Araki, T., Watson, M., and Milbrandt, J. (2001). EGR2 Mutations in Inherited Neuropathies Dominant-Negatively Inhibit Myelin Gene Expression. Neuron *30*, 355-368. 10.1016/S0896-6273(01)00282-3.
S28. Zhang, P., Chen, Y., Zhang, S., Fang, M., Lin, X., Liu, T., Zhou, Y., Yu, X., and Chen, G. (2020). Egr2 upregulation induced mitochondrial iron overload implicating in sevoflurane-induced cognitive deficits in developing mice. Preprint from Research Square. 10.21203/RS.3.RS-131690/V1.
S29. Unoki, M., and Nakamura, Y. (2003). EGR2 induces apoptosis in various cancer cell lines by direct transactivation of BNIP3L and BAK. Oncogene *22*, 2172-2185. 10.1038/sj.onc.1206222.

S30. Gradinaru, D., Minn, A.L., Artur, Y., Minn, A., and Heydel, J.M. (2012). Effect of oxidative stress on UDP-glucuronosyltransferases in rat astrocytes. Toxicol Lett *213*, 316-324. 10.1016/J.TOXLET.2012.07.014.

S31. Enenstein, J., Milbauer, L., Domingo, E., Wells, A., Roney, M., Kiley, J., Wei, P., and Hebbel, R. (2010). Proinflammatory phenotype with imbalance of KLF2 and RelA: risk of childhood stroke with sickle cell anemia. Am J Hematol *85*, 18-23. 10.1002/AJH.21558.

S32. Shi, H., Sheng, B., Zhang, F., Wu, C., Zhang, R., Zhu, J., Xu, K., Kuang, Y., Jameson, S., Lin, Z., et al. (2013). Kruppel-like factor 2 protects against ischemic stroke by regulating endothelial blood brain barrier function. Am J Physiol - Heart Circ *304*. 10.1152/AJPHEART.00712.2012.

S33. Wu, C., Li, F., Han, G., and Liu, Z. (2013). Aβ(1-42) disrupts the expression and function of KLF2 in Alzheimer's disease mediated by p53. Biochem Biophys Res Commun *431*, 141-145. 10.1016/J.BBRC.2013.01.008.

S34. Doddaballapur, A., Michalik, K.M., Manavski, Y., Lucas, T., Houtkooper, R.H., You, X., Chen, W., Zeiher, A.M., Potente, M., Dimmeler, S., and Boon, R.A. (2015). Laminar Shear Stress Inhibits Endothelial Cell Metabolism via KLF2-Mediated Repression of PFKFB3. Arterioscler Thromb Vasc Biol *35*, 137-145. 10.1161/ATVBAHA.114.304277.

S35. Maity, J., Deb, M., Greene, C., and Das, H. (2020). KLF2 regulates dental pulp-derived stem cell differentiation through the induction of mitophagy and altering mitochondrial metabolism. Red Biol *36*, 101622. 10.1016/J.REDOX.2020.101622.

S36. Yambire, K.F., Fernandez-Mosquera, L., Steinfeld, R., Mühle, C., Ikonen, E., Milosevic, I., and Raimundo, N. (2019). Mitochondrial biogenesis is transcriptionally repressed in lysosomal lipid storage diseases. eLife *8*. 10.7554/ELIFE.39598.

S37. Dempster, E., Wong, C., Lester, K., Burrage, J., Gregory, A., Mill, J., and Eley, M. (2014). Genome-wide methylomic analysis of monozygotic twins discordant for adolescent depression. Biol Psychiatry *76*, 977-983. 10.1016/J.BIOPSYCH.2014.04.013.

S38. Gasparoni, G., Bultmann, S., Lutsik, P., Kraus, T.F.J., Sordon, S., Vlcek, J., Dietinger, V., Steinmaurer, M., Haider, M., Mulholland, C.B., et al. (2018). DNA methylation analysis on purified neurons and glia dissects age and Alzheimer's disease-specific changes in the human cortex. Epigenetics Chromatin 2018 11:1 *11*, 1-19. 10.1186/S13072-018-0211-3.

S39. Starnawska, A., Hansen, C.S., Sparsø, T., Mazin, W., Olsen, L., Bertalan, M., Buil, A., Bybjerg-Grauholm, J., Bækvad-Hansen, M., Hougaard, D.M., et al. (2017). Differential DNA methylation at birth associated with mental disorder in individuals with 22q11.2 deletion syndrome. Transl Psychiatry *7*, e1221-e1221. 10.1038/tp.2017.181.

S40. Gurrapu, S., and Tamagnone, L. (2016). Transmembrane semaphorins: Multimodal signaling cues in development and cancer. Cell Adh Migr *10*, 675. 10.1080/19336918.2016.1197479.

S41. Li, H., Wu, D., and Sullivan, S. (1999). Characterization and expression of sema4g, a novel member of the semaphorin gene family. Mech Dev *87*, 169-173. 10.1016/S0925-4773(99)00125-2.

S42. Maier, V., Jolicoeur, C., H, R., Takegahara, N., Kumanogoh, A., Kikutani, H., Tessier-Lavigne, M., Wurst, W., and Friedel, R. (2011). Semaphorin 4C and 4G are ligands of Plexin-B2 required in cerebellar development. Mol Cell Neurosci *46*, 419-431. 10.1016/J.MCN.2010.11.005.

S43. Tseveleki, V., Rubio, R., Vamvakas, S.-S., White, J., Taoufik, E., Petit, E., Quackenbush, J., and Probert, L. (2010). Comparative gene expression analysis in mouse models for multiple sclerosis, Alzheimer's disease and stroke for identifying commonly regulated and disease-specific gene changes. Genomics *96*, 82. 10.1016/J.YGENO.2010.04.004.

SS44. Arenas, M., Fairbanks, L.D., Vijayakumar, K., Carr, L., Escuredo, E., and Marinaki, A.M. (2009). An unusual genetic variant in the MOCS1 gene leads to complete missplicing of an alternatively spliced exon in a patient with molybdenum cofactor deficiency. J Inherit Metab Dis *32*, 560-569. 10.1007/S10545-009-1151-7.

S45. Lee, H.-J., Adham, I.M., Schwarz, G., Kneussel, M., Sass, J.O., Engel, W., and Reiss, J. (2002). Molybdenum cofactor-deficient mice resemble the phenotype of human patients. Hum Mol Genet *11*, 3309-3317. 10.1093/HMG/11.26.3309.

S46. Mayr, S., Sass, J., Vry, J., Kirschner, J., Mader, I., Hövener, J., Reiss, J., Santamaria-Araujo, J., Schwarz, G., and Grünert, S. (2018). A mild case of molybdenum cofactor deficiency defines an alternative route of MOCS1 protein maturation. J Inherit Metab Dis *41*, 187-196. 10.1007/S10545-018-0138-7.

S47. Reiss, J., Christensen, E., Kurlemann, G., Zabot, M., and Dorche, C. (1998). Genomic structure and mutational spectrum of the bicistronic MOCS1 gene defective in molybdenum cofactor deficiency type A. Hum Genet *103*, 639-644. 10.1007/S004390050884.

S48. Grings, M., Seminotti, B., Karunanidhi, A., Ghaloul-Gonzalez, L., Mohsen, A.-W., Wipf, P., Palmfeldt, J., Vockley, J., and Leipnitz, G. (2019). ETHE1 and MOCS1 deficiencies: Disruption of mitochondrial bioenergetics, dynamics, redox homeostasis and endoplasmic reticulum-mitochondria crosstalk in patient fibroblasts. Sci Rep *9*, 1-13. 10.1038/s41598-019-49014-2.

S49. Mayr, S.J., Röper, J., and Schwarz, G. (2020). Alternative splicing of the bicistronic gene molybdenum cofactor synthesis 1 (MOCS1) uncovers a novel mitochondrial protein maturation mechanism. J Biol Chem *295*, 3029-3039. 10.1074/JBC.RA119.010720.

S50. Dong, H., Zhang, P., Song, I., Petralia, R., Liao, D., and Huganir, R. (1999). Characterization of the glutamate receptor-interacting proteins GRIP1 and GRIP2. J Neurosci *19*, 6930-6941. 10.1523/JNEUROSCI.19-16-06930.1999.

S51. Mao, L., Takamiya, K., Thomas, G., Lin, D.-T., and Huganir, R.L. (2010). GRIP1 and 2 regulate activity-dependent AMPA receptor recycling via exocyst complex interactions. Proc Nat Acad Sci U S A *107*, 19038-19043. 10.1073/PNAS.1013494107.

S52. Takamiya, K., Mao, L., Huganir, R.L., and Linden, D.J. (2008). The glutamate receptor-interacting protein family of GluR2-binding proteins is required for long-term synaptic depression expression in cerebellar Purkinje cells. J Neurosci *28*, 5752-5755. 10.1523/JNEUROSCI.0654-08.2008.

S53. Schrauwen, I., Liaqat, K., Schatteman, I., Bharadwaj, T., Nasir, A., Acharya, A., Ahmad, W., Van Camp, G., and Leal, S. (2020). Autosomal Dominantly Inherited GREB1L Variants in Individuals with Profound Sensorineural Hearing Impairment. Genes *11*, 1-18. 10.3390/GENES11060687.

S54. Schrauwen, I., Kari, E., Mattox, J., Llaci, L., Smeeton, J., Naymik, M., Raible, D.W., Knowles, J.A., Crump, J.G., Huentelman, M.J., and Friedman, R.A. (2018). De Novo variants in GREB1L are associated with non-syndromic inner ear malformations and deafness. Hum Genet *137*, 459. 10.1007/S00439-018-1898-8.

S55. Lau, S.-F., Cao, H., Fu, A.K.Y., and Ip, N.Y. (2020). Single-nucleus transcriptome analysis reveals dysregulation of angiogenic endothelial cells and neuroprotective glia in Alzheimer's disease. Proc Nat Acad Sci U S A *117*, 25800-25809. 10.1073/PNAS.2008762117.

S56. Liu, Z., Ye, X., Zhang, J., Wu, B., Dong, S., and Gao, P. (2021). Biallelic ADGRV1 variants are associated with Rolandic epilepsy. Neurol Sci 10.1007/S10072-021-05403-Y.

S57. Myers, K., Nasioulas, S., Boys, A., McMahon, J., Slater, H., Lockhart, P., Sart, D., and Scheffer, I. (2018). ADGRV1 is implicated in myoclonic epilepsy. Epilepsia *59*, 381-388. 10.1111/EPI.13980.

S58. Yan, W., Long, P., Chen, T., Liu, W., Yao, L., Ren, Z., Li, X., Wang, J., Xue, J., Tao, Y., et al. (2018). A Natural Occurring Mouse Model with Adgrv1 Mutation of Usher Syndrome 2C and Characterization of its Recombinant Inbred Strains. Cell Physiol Biochem *47*, 1883-1897. 10.1159/000491068.

S59. Minkiewicz, J., de Rivero Vaccari, J., and Keane, R. (2013). Human astrocytes express a novel NLRP2 inflammasome. Glia *61*, 1113-1121. 10.1002/GLIA.22499.

S60. Vizlin-Hodzic, D., Zhai, Q., Illes, S., Södersten, K., Truvé, K., Parris, T., Sobhan, P., Salmela, S., Kosalai, S., Kanduri, C., et al. (2017). Early onset of inflammation during ontogeny of bipolar disorder: the NLRP2 inflammasome gene distinctly differentiates between patients and healthy controls in the transition between iPS cell and neural stem cell stages. Transl Psychiatry *7*. 10.1038/TP.2016.284.

S61. Lee, K., Lee, H., Yang, C., Ko, J., Park, C., RS, W., Kim, J., Sun, W., Kim, J., Ho, W., and Lee, S. (2015). Bidirectional Signaling of Neuregulin-2 Mediates Formation of GABAergic Synapses and Maturation of Glutamatergic Synapses in Newborn Granule Cells of Postnatal Hippocampus. J Neurosci *35*, 16479-16493. 10.1523/JNEUROSCI.1585-15.2015.

S62. Longart, M., Liu, Y., Karavanova, I., and Buonanno, A. (2004). Neuregulin-2 is developmentally regulated and targeted to dendrites of central neurons. J Comp Neurol *472*, 156-172. 10.1002/cne.20016.

S63. Nakano, N., Kanekiyo, K., Nakagawa, T., Asahi, M., and Ide, C. (2016). NTAK/neuregulin-2 secreted by astrocytes promotes survival and neurite outgrowth of neurons via ErbB3. Neuroscie Lett *622*, 88-94. 10.1016/J.NEULET.2016.04.050.

S64. Yan, L., Shamir, A., Skirzewski, M., Leiva-Salcedo, E., Kwon, O.B., Karavanova, I., Paredes, D., Malkesman, O., Bailey, K.R., Vullhorst, D., et al. (2017). Neuregulin-2 ablation results in dopamine dysregulation and severe behavioral phenotypes relevant to psychiatric disorders. Mol Psychiatry *23*, 1233-1243. 10.1038/mp.2017.22.

S65. Coughlin, C.R., Swanson, M.A., Kronquist, K., Acquaviva, C., Hutchin, T., Rodríguez-Pombo, P., Väisänen, M.-L., Spector, E., Creadon-Swindell, G., Brás-Goldberg, A.M., et al. (2016). The genetic basis of classic nonketotic hyperglycinemia due to mutations in GLDC and AMT. Genet Med *19*, 104-111. 10.1038/gim.2016.74.

S66. Pai, Y.J., Leung, K.-Y., Savery, D., Hutchin, T., Prunty, H., Heales, S., Brosnan, M.E., Brosnan, J.T., Copp, A.J., and Greene, N.D.E. (2015). Glycine decarboxylase deficiency causes neural tube defects and features of non-ketotic hyperglycinemia in mice. Nat Commun *6*. 10.1038/NCOMMS7388.

S67. Freilinger, T., Anttila, V., Vries, B.d., Malik, R., Kallela, M., Terwindt, G.M., Pozo-Rosich, P., Winsvold, B., Nyholt, D.R., Oosterhout, W.P.J.v., et al. (2012). Genome-wide association analysis identifies susceptibility loci for migraine without aura. Nat Genet *44*, 777. 10.1038/NG.2307.

S68. Hamada, N., Ogaya, S., Nakashima, M., Nishijo, T., Sugawara, Y., Iwamoto, I., Ito, H., Maki, Y., Shirai, K., Baba, S., et al. (2018). De novo PHACTR1 mutations in West syndrome and their pathophysiological effects. Brain *141*, 3098-3114. 10.1093/BRAIN/AWY246.

S69. Ito, H., Mizuno, M., Noguchi, K., Morishita, R., Iwamoto, I., Hara, A., and Nagata, K.i. (2018). Expression analyses of Phactr1 (phosphatase and actin regulator 1) during mouse brain development. Neurosci Res *128*, 50-57. 10.1016/J.NEURES.2017.08.002.

S70. Garcia, J., Ferreira, H., Vieira, F., Gameiro, R., Andrade, A., Eugênio, F., Flores, E., and Cardoso, T. (2017). Tumour necrosis factor-alpha-induced protein 8 (TNFAIP8) expression associated with cell survival and death in cancer cell lines infected with canine distemper virus. Vet Comp Oncol *15*, 336-344. 10.1111/VCO.12168.

S71. Li, T., Wang, W., Gong, S., Sun, H., Zhang, H., Yang, A.-G., Chen, Y.H., and Li, X. (2018). Genome-wide Analysis Reveals TNFAIP8L2 as an Immune Checkpoint Regulator of Inflammation and Metabolism. Mol Immunol *99*, 154-162. 10.1016/j.molimm.2018.05.007

S72. Niture, S., Lin, M., Odera, J.O., Moore, J., Zhe, H., Chen, X., Suy, S., Collins, S.P., and Kumar, D. (2021). TNFAIP8 drives metabolic reprogramming to promote prostate cancer cell proliferation. Int J Biochem Cell Biol *130*, 105885. 10.1016/J.BIOCEL.2020.105885.

S73. Alcantara, D., Timms, A., Gripp, K., Baker, L., Park, K., Collins, S., Cheng, C., Stewart, F., Mehta, S., Saggar, A., et al. (2017). Mutations of AKT3 are associated with a wide spectrum of developmental disorders including extreme megalencephaly. Brain *140*, 2610-2622. 10.1093/BRAIN/AWX203.

S74. Howell, K.R., Floyd, K., and Law, A.J. (2017). PKBγ/AKT3 loss-of-function causes learning and memory deficits and deregulation of AKT/mTORC2 signaling: Relevance for schizophrenia. PLOS ONE *12*, e0175993. 10.1371/JOURNAL.PONE.0175993.

S75. Lopes, F., Torres, F., Soares, G., van Karnebeek, C.D., Martins, C., Antunes, D., Silva, J., Muttucomaroe, L., Botelho, L.F., Sousa, S., et al. (2019). The Role of AKT3 Copy Number Changes in

Brain Abnormalities and Neurodevelopmental Disorders: Four New Cases and Literature Review. Front Genet *0*, 58. 10.3389/FGENE.2019.00058.

S76. Zhang, T., Ding, H., Wang, Y., Yuan, Z., Zhang, Y., Chen, G., Xu, Y., and Chen, L. (2021). Akt3-mTOR regulates hippocampal neurogenesis in adult mouse. J Neurochem. 10.1111/JNC.15441.

S77. Kim, M., Kim, Y.Y., Jee, H.J., Bae, S.S., Jeong, N.Y., Um, J.-H., and Yun, J. (2016). Akt3 knockdown induces mitochondrial dysfunction in human cancer cells. Acta Biochim Biophys Sin *48*, 447-453. 10.1093/ABBS/GMW014.

S78. Polytarchou, C., Hatziapostolou, M., Yau, T.O., Christodoulou, N., Hinds, P.W., Kottakis, F., Sanidas, I., and Tsichlis, P.N. (2020). Akt3 induces oxidative stress and DNA damage by activating the NADPH oxidase via phosphorylation of p47(phox). Proc Natl Acad Sci U S A *117*, 28806-28815. 10.1073/pnas.2017830117.

S79. Matsui, A., Tran, M., Yoshida C., A., Kikuchi, S.S., Mami, U., Ogawa, M., and Shimogori, T. (2013). BTBD3 controls dendrite orientation toward active axons in mammalian neocortex. Science *342*, 1114-1118. 10.1126/science.1244505

S80. Thompson, S., Welch, A., Ho, E., Bessa, J., Portugal-Nunes, C., Morais, M., Young, J., Knowles, J., and Dulawa, S. (2019). Btbd3 expression regulates compulsive-like and exploratory behaviors in mice. Transl Psychiatry *9*. 10.1038/S41398-019-0558-7.